



---

**HEALTH MONITORING OF AIRCRAFT  
BY NONLINEAR ELASTIC WAVE SPECTROSCOPY**

**AERONEWS**

EC SIXTH FRAMEWORK PROGRAMME  
PRIORITY 4: AERONAUTICS AND SPACE

SPECIFIC TARGETED RESEARCH: AST3-CT-2003-502927

PROJECT WEBPAGE: <http://www.kuleuven-kortrijk.be/aeronews/>

PROJECT COORDINATOR: Prof. [KOEN VAN DEN ABEELE](#)



---

**Deliverable D6**

Support in terms of simulation models for the experimental optimization study  
envisaged in WP1

---

**Period covered: from March 1, 2004 to February 29, 2008**

Date of preparation: April 15, 2006

Update: April 15, 2008

Start date of project: March 1, 2004

Duration: 4 years (February 29, 2008)

Project coordinator name: Koen Van Den Abeele

Project coordinator organization name: KULeuven

Report authors: Polito, CU, GIP-U, KULeuven, UNIVBRIS

Final version (confidential)

## **Introduction**

Improvement of NEWS techniques can lead to a significant breakthrough in the development of new reliable and robust damage imaging systems. However, extensive theoretical studies and numerical modelling are required in order to aid the design, application and optimisation of these methodologies. To achieve these objectives, Work-Package 2 focused on (i) the development of theoretical and numerical models to simulate damage types identified in WP1, and (ii) the development of algorithms which enabled the detection of defective zones in large scale structures, localising faults and predicting their impact using NEWS measurements.

The ultimate goal of WP2 was to support experimental procedures and methodologies, providing guidance in terms of method selection, placement of sensors and actuators, and data acquisition and processing, assisting Work-Packages WP1, WP3 and WP4.

Two sub-packages were distinguished in WP2: Pure and applied modelling.

*WP2.1: Simulation Studies of damaged simple and complex components;*

*WP2.2: Damage localization procedure and NEWIMAGE.*

The objective for Deliverable D6 is to report – within WP2.1 – on the development and validation of multiscale dynamic models for damaged materials with nonlinear and hysteretic state relations at the microscale level. The work presented in Deliverable D6 was a prerequisite for WP2.2, and as such also supported experimental measurements performed in WP1.

The following tasks have been performed in WP2.1:

- Development and improvement of numerical techniques to simulate the presence of various type of damage identified in WP1;
- Development of microscale numerical models with the different damage levels and typologies identified in WP1;
- Development of theoretical models and methodologies to link microscale to mesoscale material behaviour;
- Identification of data which is sensitive to each type of damage under investigation;
- Development of methodologies for the analysis of nonlinear wave propagation for a variety of damage scenarios, as identified in WP1;
- Model verification, refinement and validation supported by experimental results (WP1) and comparisons between several numerical methods;
- Numerical studies on the theoretical resolution of NEWS techniques for damage detection in various structures and under different conditions;
- Numerical simulations to provide guidance for designing the optimal experimental set-up of emitters and sensors (WP3).

This final report on deliverable D6 contains 4 parts:

- D6.1: a description of the cases of interest for modelling
- D6.2: a description of the numerical methods used
- D6.3: results of the simulation support
- D6.4 innovative filtering techniques useful for NEWS

### **D6.1. Definition of cases of interest for modelling**

In view of the foreseen practical applications of the methodologies developed in this project, Work-Package 2 decided to focus on the description and modelling of wave propagation phenomena in composites and metals which contain a localised zone of microdamage. Damage can be in the form of a concentration of microcracks and/or defective adhesive joints. It is assumed that microdamage can be of the following types:

(a) *Inclusions with a classical nonlinear stress-strain relation.*

This type of nonlinearity can be modelled by means of a Taylor series expansion of the stress-strain relation. The constitutive equation is reversible (i.e. unique).

(b) *Inclusions with a nonclassical nonlinear (hysteretic) stress-strain relation.*

This type of nonlinearity can be modelled as a statistical ensemble of bistable units with characteristic opening and closing pressures (PM-space formalism). The corresponding stress-strain relation is non-unique and highly dependent on the history.

(c) *Inclusions with a reduced elastic modulus and increased attenuation.*

This is a ‘linear’ damage, which can be modelled by introducing heterogeneity in the elastic material constants. This type of damage is not of specific interest to this project, but is used as a reference to emphasise the sensitivity of nonlinear techniques.

Among the features which characterise the nonlinear response of micro-damage, hysteresis is one of the least understood in terms of its origin. Certainly the nature of hysteretic behaviour can be traced back to features at the mesoscopic level (therefore we speak of “mesoscopic elasticity”). In spite of the fact that the origin of hysteresis is not well known (we will give some possible mechanisms later in 2b), several numerical methods and experimental techniques have been developed for damage detection taking advantage of the hysteretic properties of damaged materials. The application of these techniques for aeronautical purposes is envisaged in WP1, whereas the numerical support is the main task of WP2.

In addition to the representation of damage as a ‘static’ material state condition, it is of particular interest for NDT and the modelling of wave propagation phenomena to gain knowledge on the *evolution* of damage states in materials, and to integrate damage progression models in the numerical simulations so that effects due to progressive damage can be predicted.

For example in metals, plastic flow and hardening are the results of the generation and motion of large numbers of discrete dislocations. The distribution and density of the dislocations influence damage initiation and evolution, the crack/void geometry and related

stress fields, the crack tip geometries, and the elastic energy dissipation. The non-uniform elastic energy dissipation as a result of damage can be related to the distribution of hysteretic features within a representative cell.

## **D6.2. Numerical methods for the simulations and underlying physics models for hysteresis**

In order to describe the macroscopic effects of microdamage on the propagation of waves in objects of finite geometry, and to be able to reconstruct the location of the damage, several numerical models have been developed and enhanced to include dynamic nonlinear (and non-unique) stress-strain relations.

### **(2a) Description of numerical methods used**

#### **KULeuven**

The numerical model used by KULeuven is a multiscale model for nonlinear wave propagation in a medium with stress-strain hysteresis. At the micro-level, microcracks were simulated by trigger-like elements with a two-state nonlinear stress-strain relation. Each hysteretic feature is described by characteristic opening and closing pressures, as indicated in Figure 2a.1. Its contribution to the strain is given by  $\gamma$ .

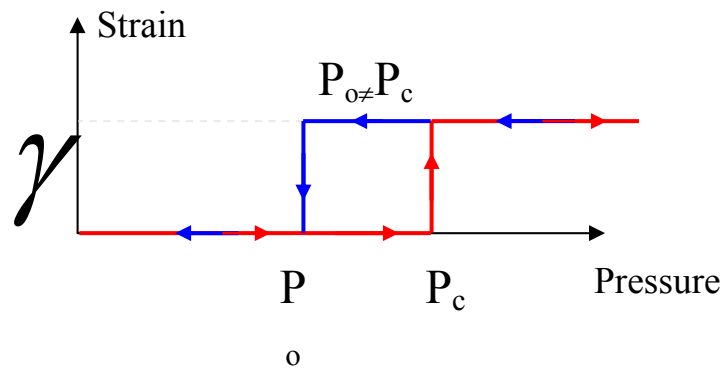


Figure 2a.1: Elementary hysteretic element (bistable unit) used to describe microdamage

We upscale the hysteretic microscopic state relation to the mesoscopic level by means of a scalar Preisach-Mayergoyz (PM) approach. This is a statistical ensemble of a large number of bistable features with differing opening and closing pressures. For multidimensional hysteretic elasticity, this approach is generalized by decomposing the stress tensor in its eigenstress components and associating a scalar PM-space to each eigenstress component. In addition, we can also introduce classical nonlinearity (in general  $K_c(\sigma)$ ), and heterogeneity in the ‘linear’ elastic material parameters at the mesoscopic level. For a given stress protocol and known PM density distribution, it is straightforward to predict the strain response of a cell using the infinitesimal  $(\Delta\sigma, \Delta\varepsilon)$  relation:

$$\Delta\varepsilon = \Delta\varepsilon_C + \Delta\varepsilon_H = \int_{-\sigma-\Delta\sigma}^{-\sigma} \frac{d\sigma'}{K_C(-\sigma')} + \gamma N (f_c(-\sigma) - f_c(-\sigma - \Delta\sigma))$$

Here  $f_c$  is the fraction of features which are closed at the current pressure level ( $N$  is the total number of hysteretic features). The procedure involves a careful administration of the open and closed units in the PM-space and a proper numerical integration. As a consequence we arrive at the following expression for the (inverse) modulus:

$$K^{-1} = \lim_{\Delta\sigma \rightarrow 0} \left( \frac{\Delta\varepsilon}{\Delta\sigma} \right) = \frac{1}{K_C(-\sigma)} + \gamma N \frac{df_c}{d\sigma}(-\sigma).$$

Using this expression, we then input this in a staggered grid EFIT formulation to predict the macroscopic response of the sample to an arbitrary excitation signal. This leads to the following finite difference equations (case 2D wave propagation and square grid):

$$\begin{aligned} \dot{v}_x^{(n,m)}(t) &= \frac{1}{\Delta x} \frac{2}{\rho^{(n,m)} + \rho^{(n+1,m)}} (T_{xx}^{(n+1,m)}(t) - T_{xx}^{(n,m)}(t) + T_{xy}^{(n,m)} - T_{xy}^{(n,m-1)}) \\ \dot{v}_y^{(n,m)}(t) &= \frac{1}{\Delta x} \frac{2}{\rho^{(n,m)} + \rho^{(n,m+1)}} (T_{yy}^{(n,m+1)}(t) - T_{yy}^{(n,m)}(t) + T_{xy}^{(n,m)} - T_{xy}^{(n-1,m)}) \\ \dot{T}_{xx}^{(n,m)}(t) &= \frac{1}{\Delta x} K_1^{(n,m)} [v_x^{(n,m)}(t) - v_x^{(n-1,m)}(t)] + \frac{1}{\Delta x} K_2^{(n,m)} [v_y^{(n,m)}(t) - v_y^{(n,m-1)}(t)] \\ \dot{T}_{yy}^{(n,m)}(t) &= \frac{1}{\Delta x} K_1^{(n,m)} [v_y^{(n,m)}(t) - v_y^{(n,m-1)}(t)] + \frac{1}{\Delta x} K_2^{(n,m)} [v_x^{(n,m)}(t) - v_x^{(n-1,m)}(t)] \\ \dot{T}_{xy}^{(n,m)}(t) &= \frac{1}{\Delta x} \frac{4}{\frac{1}{\mu^{(n,m)}} + \frac{1}{\mu^{(n+1,m)}} + \frac{1}{\mu^{(n,m+1)}} + \frac{1}{\mu^{(n+1,m+1)}}} [v_x^{(n,m+1)}(t) - v_x^{(n,m)}(t) + v_y^{(n+1,m)}(t) - v_y^{(n,m)}(t)] \end{aligned}$$

The values of  $K_1$ ,  $K_2$  and  $\mu$  need to be updated at each time-step because of the amplitude and history dependence of the moduli in a nonlinear system. Linear material attenuation can be accounted for by introducing a chain of relaxation mechanisms.

The code has been developed for 1D, 2D and 3D cases. KULeuven also has a code for flexural waves starting from the 1D Euler-Bernoulli equation.

## POLITO

The model used by POLITO to simulate the presence of damage in nonclassical nonlinear materials is based on the Local Interaction Simulation Approach (LISA), developed by this group in the past 15 years represents a special (*ad hoc*) version of Finite Difference (FD) method. In one dimension (the extension to higher dimension is straightforward), the specimen is discretized in elastic elements (“cells”) and the nonlinearity is introduced by including nontrivial boundary conditions on each element. This is obtained by defining thin space regions called Hysteretic Mesoscopic Units (HMU), which behave either rigidly or elastically, depending on the local pressure. A rigid HMU corresponds to imposing continuity of stresses and displacements between cells, i.e. absence of defects. Elastic

HMU's describe linear inclusions or delaminations. HMU's switching from a rigid to an elastic state and *vice versa* during the crossing of the propagating wave describe a nonlinear inclusion. The cells are described, as usual, by the linear constitutive stress-strain ( $\sigma - \varepsilon$ ) relation:

$$\sigma = K\varepsilon$$

where  $K$  is the Young's modulus. In order to model the transitions between the two states of the regions with nonlinear hysteretic properties a PM-space approach is adopted. We suppose that each "physical mesoscopic" nonlinear unit of the specimen corresponds to a point in the PM-space and is described by a two state element, characterised by different equations of state. The sudden transition between the states is driven by an external variable, which is usually chosen as the stress. In our approach we assign different elastic properties to the two states (see Fig 2a.2b). The constitutive equation for the nonlinear unit is defined as:

$$\tau = \alpha P + \beta \eta + \gamma \dot{\eta}$$

where  $\tau$  and  $\eta$  represent the HMU's stress and strain respectively,  $P$  is the pressure applied on the HMU and  $\alpha$ ,  $\beta$  and  $\gamma$  are constants. The dot represents a derivative in time. The condition of rigid state (intact) is achieved by imposing  $\{\alpha, \beta, \gamma\} = \{\alpha_1, \beta_1, \gamma_1\} = \{0.5, 0, \forall\}$ . Values of the parameters such as  $0 < \alpha < \alpha_1$  and  $\beta > \beta_1$  give an elastic state. The nonlinear effects increase, for example, increasing the distance of  $\alpha$  from  $\alpha_1$ , i.e. the distance of the elastic state from the rigid one.

From the stress-strain relation we obtain as usual the differential equations describing the temporal evolution of both cells and HMU's. Then we solve the differential equation by means of the standard iterative procedure of the FD method.

### GIP-U

GIP-U has developed 1D, 2D and 3D pseudo-spectral time domain algorithms (PSTD) for solving elastic wave equation in nonlinear hysteretic heterogeneous solids using FFTs for calculation of the spatial differential operator on staggered grid:

$$\frac{\partial f(x, y, t)}{\partial x} = FFT^{-1} \left[ \left( jk_x e^{\pm jk_x \frac{\Delta x}{2}} \right) FFT[f(x, y, t)] \right] \quad (1)$$

where  $FFT^{-1}$  is the inverse Fast Fourier Transform and  $k_x$  is the wave number in  $x$  direction.  $\Delta x$  is the spatial step of the numerical grid in  $x$  direction. To reduce numerical artifacts in pseudospectral simulations for a heterogeneous medium, a staggered spatial grid implementation is used. Moreover, a staggered fourth-order Adams-Bashforth method is used to update stress and particle velocity at alternating half time steps. The main advantage of this method for nonlinear elastic wave simulation is that only two node points are needed per minimum wavelength, even for long time propagation. In this case, where frequencies up to the fifth harmonic are considered, only ten node points per wavelength are enough. This can be compared to the almost fifty node points which are needed in

Finite Element (FE) or Finite Difference Time Domain (FDTD) methods. To circumvent wraparound inherent to FFT-based pseudo-spectral simulation, a novel implementation of Perfectly Matched Layers (PML) boundary condition named convolutional PML (CPML) has been used.

Hysteretic nonlinearity is introduced with the multiscale PM space model introduced by KULeuven. In this model, no analytical expression of the bulk modulus is given. It is calculated by summation of the strain contribution of a numerous number of elementary hysteretic elements. Each hysteretic element unit (HEU) is described by two characteristic stresses  $P_c$  and  $P_o$ , corresponding to the transition between two states when the stress is increased or decreased, respectively. One state corresponds to an “open” state and the other one to a “closed” state. For each cell of the calculation grid (representing a mesoscopic level of the medium description),  $N_0$  hysteretic units are considered with different values of the two stresses characteristic. Two kind of elementary hysteretic elements have been considered here, as shown on Figure 1. The first model (a) corresponds to the one used by KULeuven, and the second one (b) (for  $\gamma_2 = 0$ ) to the model introduced by POLITO.

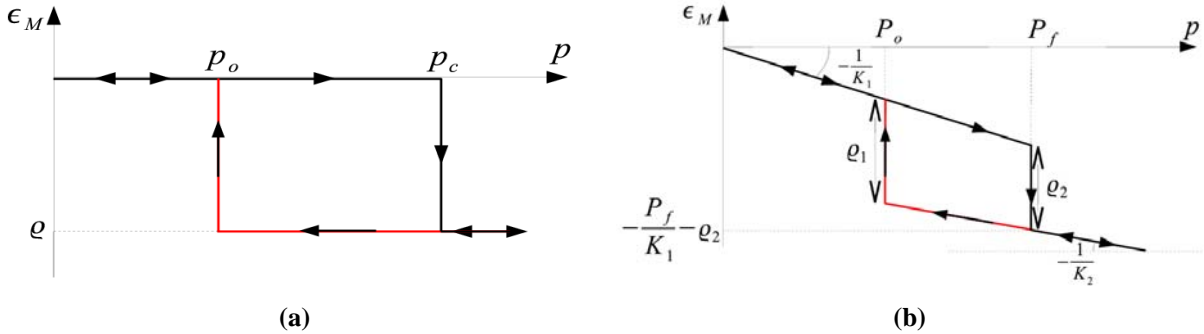


Figure 2a.2: Elementary hysteretic elements used in the computation of the « PM » space model. (a) “inelastic” two states element, and (b) “elastic” two states element.

Considering the propagation of elastic waves in a heterogeneous solid, Newton’s second law can be written:

$$\frac{\partial v_i}{\partial t} = \frac{1}{\rho_0} \frac{\partial \tau_{ij}}{\partial x_j}, \quad (2)$$

where  $x_j$  are the components of the position vector,  $\rho_0$  is the density,  $v_i$  are the components of the particle velocity vector,  $\tau_{ij}$  are the components of the stress tensor and  $t$  is time. The constitutive equation for a linear elastic solid is given by the Hooke’s law:

$$\tau_{ij} = C_{ijkl} \epsilon_{kl}, \quad (3)$$

where  $\epsilon$  is the strain tensor and  $C_{ijkl}$  are the elastic coefficients. Here the propagation of P-SV waves in 2D transverse isotropic solid is considered where the stress – strain relation is given by:

$$\begin{pmatrix} \tau_{xx} \\ \tau_{zz} \\ \tau_{xz} \end{pmatrix} = \begin{pmatrix} C_{11} & C_{13} & 0 \\ C_{13} & C_{33} & 0 \\ 0 & 0 & C_{44} \end{pmatrix} \begin{pmatrix} \epsilon_{xx} \\ \epsilon_{zz} \\ \epsilon_{xz} \end{pmatrix} \quad (4)$$

where the elastic matrix is given in the Voigt notation. The 2D elastic wave solver used in this study is based on a Kelvin notation method. Using this notation, the 3 eigenvectors of the elastic constants tensor (in 2D) correspond to 3 eigenstress / eigenstrain vectors. These vectors represent directions where applied stress and response strain are in the same direction. Doing so, it is possible to use for each of these 3 directions a scalar “PM space” model similar to the one shown on Figure 1. Each PM space associated with the different directions modifies the associated eigenstiffness.

➤ Kelvin notation in 2D

To take into account the induced anisotropy by nonlinear effect, we consider first the propagation in 2D transverse isotropic solid. In such solid, the propagation of P-S<sub>V</sub> waves can be decoupled from the propagation of S<sub>H</sub> waves. Based on these Kelvin notations, the stresses calculation steps are as follow:

1. Calculation of the 2D Kelvin stress vector:

$$\tilde{\tau}_{xx} = \tau_{xx}, \tilde{\tau}_{zz} = \tau_{zz}, \tilde{\tau}_{xz} = \tau_{xz} \sqrt{2}. \quad (5)$$

2. Calculation of the projections of the stresses along the 3 Eigenstress directions:

$$\tilde{\tau}^{(1)} = \frac{X_1}{\sqrt{1+X_1^2}} \tau_{xx} + \frac{1}{\sqrt{1+X_1^2}} \tau_{zz}, \quad \tilde{\tau}^{(2)} = \frac{X_2}{\sqrt{1+X_2^2}} \tau_{xx} + \frac{1}{\sqrt{1+X_2^2}} \tau_{zz}, \quad \tilde{\tau}^{(3)} = \tau_{xz} \sqrt{2} \quad (6)$$

where:  $X_1 = -\frac{1}{C_{13}} \left( \frac{C_{33}}{2} - \frac{C_{11}}{2} - \Delta C \right)$ ,  $X_2 = -\frac{1}{C_{13}} \left( \frac{C_{33}}{2} - \frac{C_{11}}{2} + \Delta C \right)$ ,  $\alpha_1 = \frac{C_{33}}{2} + \frac{C_{11}}{2} + \Delta C$ ,  
 $\alpha_2 = \frac{C_{33}}{2} + \frac{C_{11}}{2} - \Delta C$ , and  $\Delta C = \frac{1}{2} \sqrt{C_{33}^2 - 2C_{11}C_{33} + C_{11}^2 + 4C_{13}^2}$ .

3. Modification of each associated eigenvalue  $E^{(i)}$  using a scalar PM space model.

$$E^{(1)} = \frac{1}{\frac{1}{\alpha_1} + \gamma_1 \frac{\partial \tilde{\mathcal{E}}_H^{(1)}}{\partial \tilde{\tau}^{(1)}}}, \quad E^{(2)} = \frac{1}{\frac{1}{\alpha_2} + \gamma_2 \frac{\partial \tilde{\mathcal{E}}_H^{(2)}}{\partial \tilde{\tau}^{(2)}}}, \quad E^{(3)} = \frac{1}{\frac{1}{2C_{44}} + \gamma_3 \frac{\partial \tilde{\mathcal{E}}_H^{(3)}}{\partial \tilde{\tau}^{(3)}}}. \quad (7)$$

4. Calculation of the modified elastic tensor using the relations:

$$C_{11} = E^{(1)} \frac{X_1^2}{1+X_1^2} + E^{(2)} \frac{X_2^2}{1+X_2^2}, \quad C_{13} = E^{(1)} \frac{X_1}{1+X_1^2} + E^{(2)} \frac{X_2}{1+X_2^2},$$

$$C_{33} = E^{(1)} \frac{1}{1+X_1^2} + E^{(2)} \frac{1}{1+X_2^2}, \quad C_{44} = \frac{E^{(3)}}{2}. \quad (8)$$

➤ Kelvin notation extension in 3D

The pseudo-spectral time domain algorithm has been extended in 3D to be able to simulate problems of wave propagation in samples with simple geometry, but with hysteretic nonlinearity. Using the same Kelvin formalism applied to 2D, 3D eigenstresses and eigenstrains have been calculated. The hysteretic nonlinear behaviour is modelled by the same multi-scale Preisach-Mayergoz (PM) model (Figure 1). Elastic constants are calculated at each time step adding contributions of a great number of hysteretic elementary units (HEU) to the deformation imposed by the wave.

Generally when nonlinear effects are considered, even in the case of classical nonlinearity, an elastic wave propagating in a medium induces a certain level of anisotropy. For example, it is well known that when the so called geometric nonlinearity (e.g. the nonlinearity of strain-displacement relations) is considered, then the problem of nonlinear propagation in isotropic solids is rewritten as a linear problem with effective elastic coefficients (dependent on displacements) and these coefficients do not have the symmetry  $C_{ijkl} = C_{jikl}$ . In this case, the Voigt and Kelvin notations of the tensor of elastic coefficients cannot be used. In our case, since we consider only highly nonlinear zones, the geometrical nonlinearity is negligible in comparison with that of the stress-strain relation. Moreover, due to the geometry of the considered cracks (penny shape), we suppose that the effective medium of the cell in which a crack is located has a transverse isotropic behaviour. So in the case of a crack oriented perpendicularly to the z-axis, the tensor of effective elastic coefficients in Kelvin notation is given by:

$$\tilde{C}_{IJ} = \begin{pmatrix} C_{11} & C_{12} & C_{13} & 0 & 0 & 0 \\ C_{12} & C_{11} & C_{13} & 0 & 0 & 0 \\ C_{13} & C_{13} & C_{13} & 0 & 0 & 0 \\ 0 & 0 & 0 & 2C_{44} & 0 & 0 \\ 0 & 0 & 0 & 0 & 2C_{44} & 0 \\ 0 & 0 & 0 & 0 & 0 & 2C_{66} \end{pmatrix} \quad (9)$$

For cracks with other orientations, a rotation matrix is required to make the transformation from sample coordinates to a coordinate linked to the direction orthogonal to the crack. Using these notations, it can be shown that the six eigenvectors of the elastic constants tensor correspond to six eigenstress/eigenstrain vectors. These vectors represent directions where applied stress and generated strain are in the same direction, and are given by:



**CU**

To simulate the presence of damage in non classical nonlinear materials in 1D and 2D structures an ad-hoc FE code was developed by Cranfield University. An explicit direct integration of the equation of motion (Eq. 2a.1) was employed:

$$[M]\{\ddot{d}\}_n + [D]\{\dot{d}\}_n + [K]\{d\}_n = \{R^{ext}\}_n \quad [2a.1]$$

where  $[M]$ ,  $[D]$  and  $[K]$  are respectively the mass, damping and stiffness matrix of the structure,  $\{d\}_n$  is the displacement vector at the  $n^{\text{th}}$  time step, and  $\{R^{ext}\}_n$  is the external force vector at the  $n^{\text{th}}$  time step. By evaluating the first and the second derivatives of  $\{d\}_n$  using a central difference method and a lumped mass matrix, the motion equation 2a.1 can be explicitly solved as:

$$\frac{1}{\Delta t^2} [M]\{d\}_{n+1} = \{R^{ext}\}_n - [K]\{d\}_n + \frac{1}{\Delta t^2} [M] \left( (d)_n + \Delta t \{\dot{d}\}_{n-\frac{1}{2}} \right) - [C]\{\dot{d}\}_{n-\frac{1}{2}} \quad [2a.2]$$

with

$$\{\dot{d}\}_{n-\frac{1}{2}} = \frac{1}{\Delta t} (\{d\}_n - \{d\}_{n-1}) \quad [2a.3]$$

In order to guarantee the stability of the solution process, the integration time step  $\Delta t_{act}$  was evaluated as the product of the Courant number  $C_n$  and the smallest time step permitted  $\Delta t$  (2a.5):

$$\Delta t_{act} = C_n \Delta t \quad [2a.4]$$

$$\Delta t = \frac{L}{2c} \quad c = \sqrt{\frac{E}{\rho}} \quad [2a.5]$$

where  $L$  is the smallest element effective diameter or critical element size,  $c$  is the P-wave speed dependent on the material elastic modulus  $E$ , and density  $\rho$ . The non linear behaviour of the material was evaluated by considering the stiffness matrix forces  $[K]\{d\}_n$  of Eq. 2a.1 as sum of a linear elastic contribution  $[K_E]\{d\}_n$  (constant) and a nonlinear internal force  $\{R_e^{int}\}_n$  (see Eq. 2a.6, updated at each time step  $n$  for each element  $e$ ):

$$\{R_e^{int}\}_n = \int_{V_e} [B]^T \{\sigma\}_n dV \quad [2a.6]$$

where  $[B]$  is the strain displacement matrix,  $\{\sigma\}_n$  is the element stress vector, and  $V_e$  is the element volume. The stress vector  $\{\sigma\}_n$  was estimated as:

$$\{\sigma\}_n = [E]_n \{\varepsilon\}_n \quad \{\varepsilon\} = [B]\{d\}_n - \{\varepsilon^{in}\} \quad [2a.7]$$

with  $\{\varepsilon^{in}\}$  initial or thermal strains and  $[E]_n$  elastic matrix at the time step  $n$ . The elastic matrix coefficients were evaluated using the PM-space non classical nonlinear material model.

For three-dimensional (3D) finite element simulations Cranfield University has developed an alternative nonclassical nonlinear material formulation. This model is based on a PM-space ensemble of bistable hysteretic units with jumps in strain, as illustrated in Figure 2a.3 (a). It assumes an infinite number of units uniformly distributed over the PM-space. The two possible states of strain are  $(\varepsilon_c, \varepsilon_o)$ , so the units differ from one another only by their triggering stresses  $(\sigma_c, \sigma_o)$ . Although this formulation of bi-stable unit corresponds to a *prescribed stress* configuration, an iterative algorithm has been developed so that the input to the PM-space is the strain and the output is the corresponding stress, which facilitates the implementation in explicit finite element codes.

Therefore, the parameters defining the PM-space are the ‘closed’ and ‘open’ state strains  $(\varepsilon_c, \varepsilon_o)$ , as well as the minimum and maximum stresses for the space  $(\sigma_{\min}, \sigma_{\max})$ . For small strains characteristic of acoustic excitations, it is reasonable to assume a symmetric PM-space, i.e.  $\varepsilon_o = -\varepsilon_c$  and  $\sigma_{\max} = -\sigma_{\min}$ .

The bistable units represent features at the mesoscale level resulting from material damage (e.g. fatigue microcracking, corrosion damage etc.). In the macroscopic level of the finite elements used in the present work (which vary from  $0.125 \text{ mm}^3$  to  $1 \text{ mm}^3$  in volume, depending on the study), contributions from undamaged elastic material are added to the overall stiffness of the element as shown by the 1D springs model of Figure 2a.3 (b).

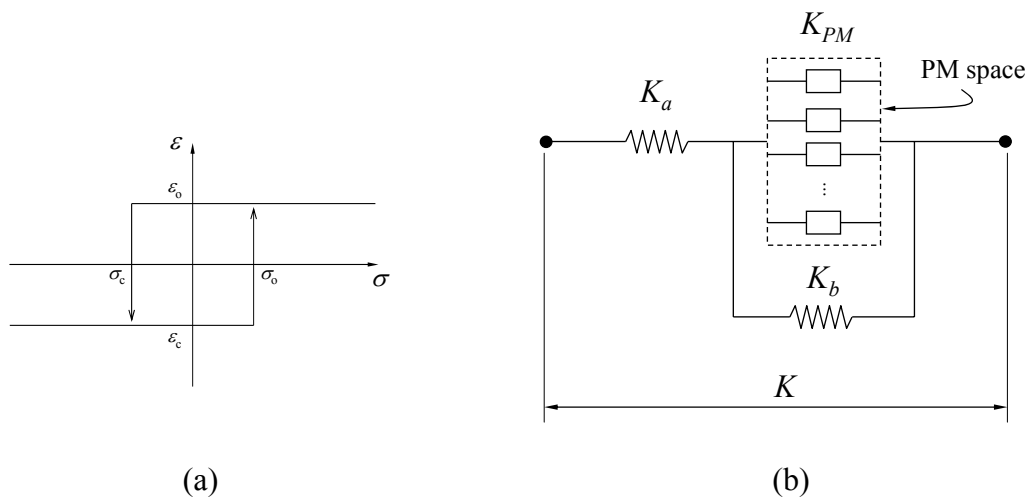


Figure 2a.3: Strain-stress relation for a single bistable hysteretic unit (a), and ensemble of units together with macroscopic elastic contributions (b).

Changes in the input strain  $\varepsilon$  will affect the bi-stable units and modify the PM-space modulus,  $K_{PM}$ , which is obtained by integration of all units (note that  $K_{PM}$  is a function of the sign of the strain rate  $\dot{\varepsilon}$ , the fraction of ‘closed’ units and the past history of  $\varepsilon$  as usual). The elastic moduli  $K_a$  and  $K_b$  are contributions of undamaged material which result in series and parallel associations with  $K_{PM}$ , respectively. Both  $K_a$  and  $K_b$  may be defined linear-elastic or classical nonlinear. The overall stiffness  $K$  is therefore given by,

$$K^{-1} = \frac{1}{K_a} + \frac{1}{K_b + K_{PM}} \quad [2a.8]$$

Figure 2a.4 (a) shows the resulting 1D stress-strain curve with a damped sinusoidal strain input and arbitrary material constants only to provide an illustration ( $K_a = 70$  GPa,  $K_b = K_a/2$ ,  $\varepsilon_o = -\varepsilon_c = 2 \cdot 10^{-5}$ ,  $\sigma_{\max} = -\sigma_{\min} = 5$  MPa). The dashed diagonal line shows the elastic output for a linear material ( $K = K_a = 70$  GPa) for comparison.

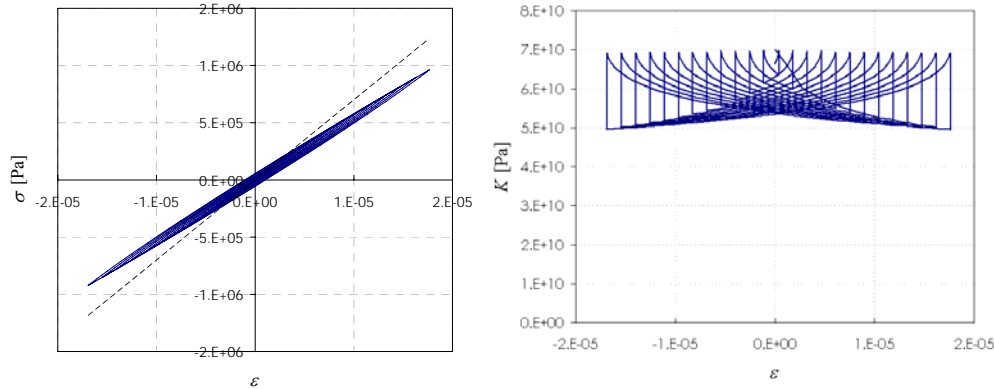


Figure 2a.4: Example of stress-strain behaviour in 1D: (a) stress-strain curve and (b) modulus-strain curve.

Figure 2a.4 (b) shows the respective modulus-strain curve. One can readily identify the bow-tie shape characteristic of the PM-space formalism. However, in contrast with the usual PM-space formulation, this model provides well defined maximum and minimum moduli.

For the simple PM-space ( $K_{PM}$ ), the maximum theoretical modulus relates to an *inversion* in the sign of  $\dot{\varepsilon}$  followed by a *very small* change in stress, resulting in the switching of only a few hysteretic units. As a consequence of the discontinuity in the stress-strain response of these bi-stable units, the effective PM-space modulus tends to infinity when the number of switching units is small, i.e. for  $\Delta\varepsilon \rightarrow 0$ ,  $K_{PM} \rightarrow \infty$ . Conversely, the minimum modulus occurs for an infinitely large strain increment, so when  $\Delta\varepsilon \rightarrow \infty$ ,  $K_{PM} \rightarrow 0$ . Therefore, from equation [2a.8] the maximum and minimum tangent moduli (when the macroscopic elastic contribution is included) become,

$$K^{\max} = K_a \quad \text{and} \quad K^{\min} = \left( \frac{1}{K_a} + \frac{1}{K_b} \right)^{-1} \quad [2a.9]$$

Classical nonlinearity is introduced in the model by considering that both ‘macroscopic’ elastic moduli  $K_a$  and  $K_b$  arise from nonlinear elastic material which behave according to the traditional power-series expansion of Hooke’s law. We assume that both moduli are equal since they correspond to material in a similar level of damage and we truncate the power-series to the third order (in terms of stress-strain), obtaining,

$$K_a = K_b = K_0(1 - \beta\varepsilon - \delta\varepsilon^2), \quad [2a.10]$$

where  $K_0$  is the elastic modulus of undamaged material,  $\beta$  and  $\delta$  are the second and third order nonlinearity parameters, respectively.

Assuming that these properties are independent of direction (i.e. the material is isotropic), the constitutive relation of this new mesoscopic material model is defined solely by the Young's modulus  $K_0$ , the Poisson's ratio  $\nu$ , the classical nonlinear parameters  $\beta$  and  $\delta$  and the PM-space parameters  $\varepsilon_0$  and  $\sigma_{\max}$ . Examples of resulting modulus-strain curves for different combinations of material parameters are shown in Figure 2a.5. This model allows the representation of linear elasticity, classical nonlinearity, nonclassical nonlinearity or a combination of these in a robust numerical formulation.

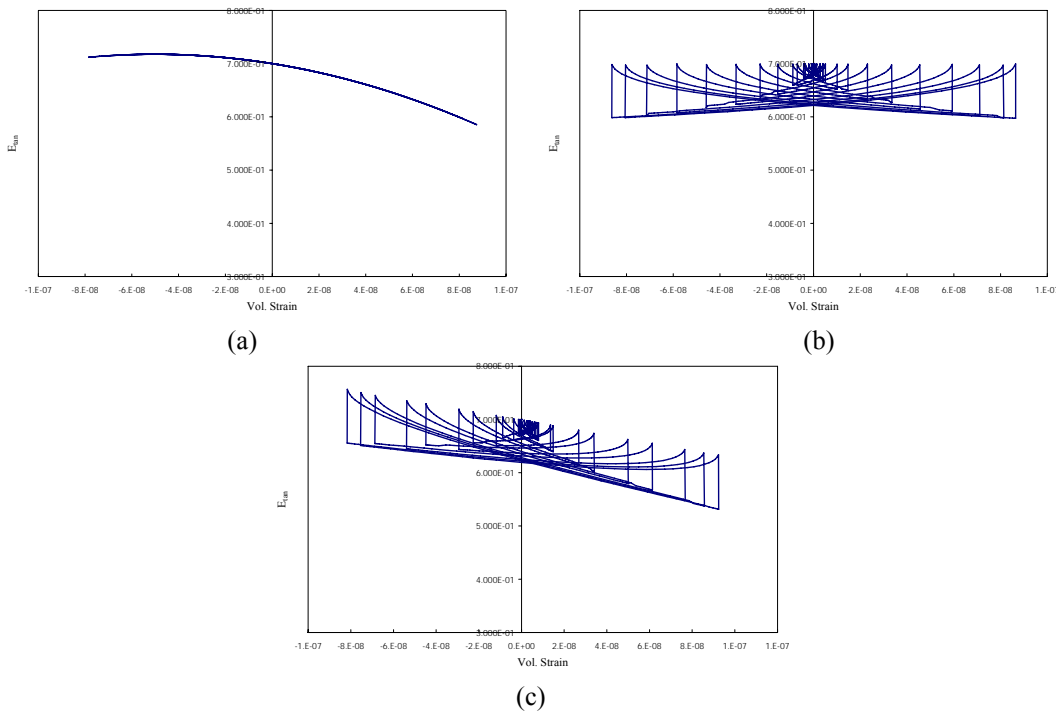


Figure 2a.5: Examples of modulus-strain behaviour for materials with (a) classical nonlinearity, (b) nonclassical nonlinearity and (c) classical-nonclassical nonlinearity.

This scalar model was introduced in the stress update algorithm for 3D solid elements in a modified version of the explicit finite element code DYNA3D. The switching of hysteretic units is controlled by changes in volumetric strain, and the resulting tangent modulus  $K$  modifies all components of the stiffness matrix for this material, according to a standard isotropic elastic element formulation.

## UNIVBRIS

The University of Bristol performed modelling in support of the ultrasonic modulation technique being developed here, in accordance with Deliverable D6. Two modelling approaches were used to support experimental work: a simple bilinear spring model

provided test data from a non-linear system with which to test and optimise signal processing methods, and linear (finite element) models were used to analyse the high order resonances that were excited by the continuous signals used. A simple bilinear spring model has proven surprisingly helpful in optimising our bispectral analysis of experimental results and revealing how the bispectrum of a non-linear system excited with the superposition of two high frequency sinusoids behaves. In particular the relationship between an experimentally interesting bispectrum peak and the excitation amplitude has been discovered, and confirmed experimentally, indicating the most useful excitation to use and providing a useful normalisation method.

A simple model has been developed to allow the optimisation of the parameters used in the bispectral analysis of samples excited by high frequency signals.

The crack is treated as a bilinear spring of stiffness  $K$ :

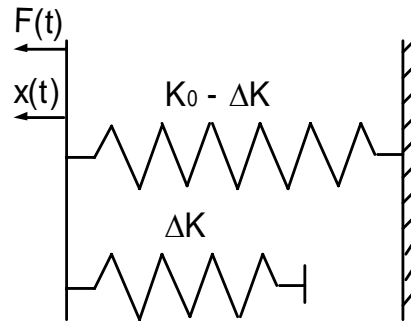
$$\begin{aligned} K(F) &= K_0; & F(t) < 0 \\ &= K_0 - \Delta K & F(t) \geq 0 \end{aligned}$$

where  $F(t)$  is the force at the crack.

$$F(t) = A_0[\sin(2\pi F_1 t + \phi_1) + \sin(2\pi F_2 t + \phi_2)].$$

The output from the system is the displacement of the surface excited by  $F(t)$ :

$$x(t) = F(t) / K(F)$$



When finding the best parameters for the bispectrum calculations noise was artificially added at -10dB (large compared to experimentally observed noise).

A commercial finite element package (ABAQUS) was used to model the original  $60\text{mm} \times 60\text{mm} \times 400\text{mm}$  steel bars in order to gain approximate resonance frequencies and mode shapes. An experiment using narrow ( $6\text{mm} \times 5\text{mm}$  cross section) samples was proposed to ensure straightforward comparison of models and experimental results. The cross-section being less than the wavelengths of the excited waves was to ensure that only longitudinal waves would be excited allowing for more straightforward analysis of propagation and behaviour at the crack. These sample were modelled in three dimensions using the commercial package and also with a one-dimensional FE model solved in Matlab.

## (2b) Physical micro-models to link different scales

As mentioned in Section 1, the origin of hysteresis is not yet fully understood. Certainly it has to be traced back to features at the mesoscopic level. The connection of the

macroscopic model parameters (and/or of the experimentally observed damage indicators) to mesoscopic/microscopic features directly indicating the structural integrity of the specimen under investigation is an important issue. Indeed, one of the steps to be accomplished is the link between the models used to describe the macroscopic propagation of waves in hysteretic elastic media and the underlying physics based theories in which features of damage appear explicitly and quantitatively. Several possible mechanisms have been proposed by WP2 partners during the first phase of the project, as discussed below.

KULeuven initially developed a physics based model form for the potential energy of crack networks to explain the hysteretic elastic behaviour of micro-cracked materials. Starting from a random collection of non-interacting micro-cracks with rough surfaces it was found that the micropotential consists of three terms: the strain energy of the surrounding intact material, the adhesive potential of the crack surfaces and an additional stabilizing contribution due to the cracks tips. Under certain conditions, the potential contains two separated minima, representing a bi-stable system. Stress-strain hysteresis is found to result from transitions in the double-well potential due to external impact, and can be linked to the Preisach-Mayergoyz (PM) formalism, yielding predictions of static and dynamic nonlinearity. The principal difference between the proposed approach and phenomenological models is that the parameters of hysteretic elements and their distributions are not arbitrary but are deduced from an analysis of the micro-geometry of the crack network. The most important geometrical parameters necessary for this description are the average area of cracks per unit of volume, and the distribution of asperities and rest apertures over the crack network.

A second physical model for the acoustical nonlinearity of micro-damaged solids developed by the KULeuven combines three independent branches of physics: tribology which studies surface forces at nanoscopic level, contact mechanics of rough surfaces, and elasticity theory for materials containing cracks. The resulting theory provides a physical basis for phenomenological approaches dealing with hysteretic nonlinearity; It is based on the hysteretic force-displacement relationship of individual asperities in contact, in which the hysteresis is attributed to the adhesion of microcontacts and the formation of necks (JKRS adhesion, see figure 2b.1).

In this framework, the hysteretic units are not the cracks themselves (as in the micropotential model), but the asperities in the cracks due to the roughness of the surfaces. Using statistics on the rough surface it is possible to determine the distribution of hysteretic units for an individual penny-like cut or crack (intergranular contacts) and for a statistical ensemble with isotropic orientation. Despite the fundamental character of these assumptions, the qualitative agreement with known experimental results is satisfactory. The resulting stress-strain relationships have close resemblance to the phenomenological Preisach-Mayergoyz model adopted for mechanical hysteresis and nonlinearity. The model also provides an explanation for a frequently observed thresholding behaviour at low strain values, and can be extended to explain observations of slow dynamical effects.

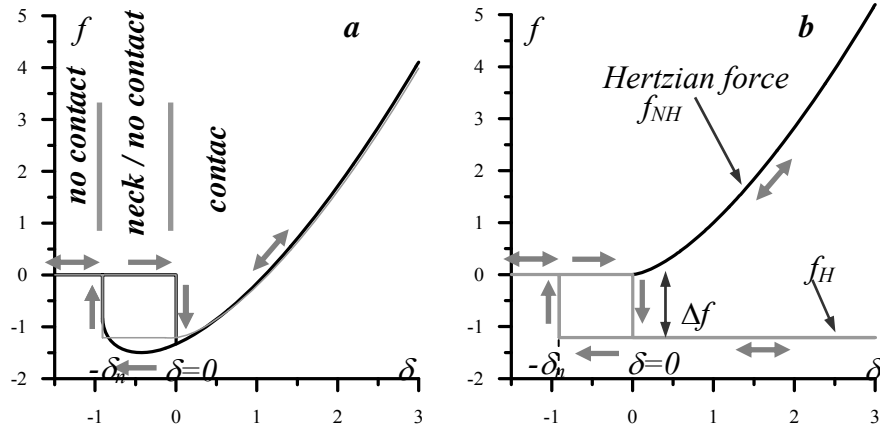


Figure 2b.1. a) JKR contact mechanics: the thick black line shows the force-displacement relationship  $f(\delta)$  with hysteresis. While increasing the displacement from highly negative interference values, there is no contact and no force. At zero interference, the contact suddenly appears with a negative force (adhesive attraction). Subsequently, for positive interferences, the contact remains. For the decreasing movement, nothing special happens until  $\delta=0$ . At that occurrence, a neck is formed, and the “contact” remains till it breaks at some negative value  $\delta=-\delta_n$  (shown by the arrows). The thin gray line indicates the simplified hysteretic dependence on top of the true JKRS model. b) The simplified hysteretic (gray) and the non-hysteretic (Hertzian, black line) force components are shown separately.

Along the same lines POLITO investigated the hysteretic properties emerging from a micromechanical model for rough surfaces in contact using a modified Greenwood-Johnson model. The model is based on the GJ description of the contact between two spherical bodies interacting via both elastic forces and forces of adhesion. The behaviour of a rough surface subject to loading has been studied through a statistical superposition of contacts (asperities) distributed according to given experimentally observed distributions of the curvature radii and of the distance between the peaks of the asperities in the absence of the external loading. As a result, hysteresis is an emergent property (see figure 2b.2).

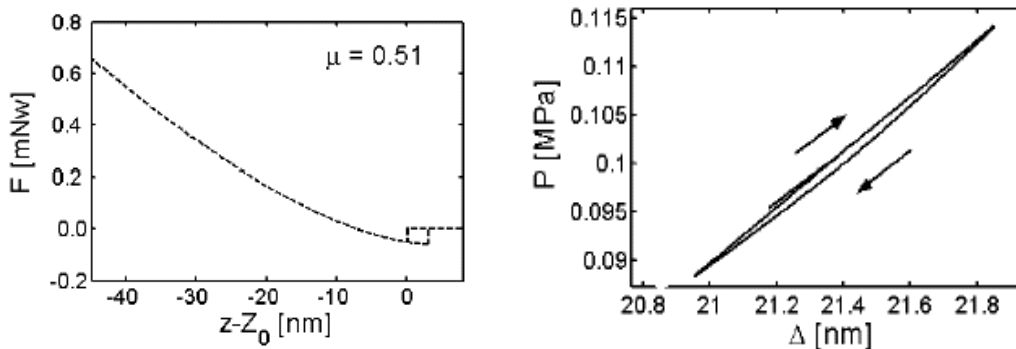


Figure 2b.2: left plot: force vs. relative approach for two asperities in contact in the GJ model; right plot: pressure vs. approach for a rough surface described as a statistical ensemble of several asperities in contact

For larger strain values (quasi-static type of experiments in which the typical deformation of the crack surfaces is higher than the characteristic asperity size), KULeuven proposed a physical tensorial stress-strain model, based on the consideration of plain cracks with friction. To do this, they combined known relations for normal displacements of crack faces given by contact mechanics, the classical Amonton's law of dry friction for lateral displacements, and the equations of elasticity theory for a collection of non-interacting cracks with given orientation. The major advantages of this model consist in the full tensorial representation, the realistic stress-strain curves for uniaxial compression and quantitative comparison with experimental data, and a profound account for hysteretic memory effects.

The conclusion of this study is that both adhesion and friction are responsible for the nonlinearity in the acoustical and elastic properties of solids with internal microstructure.

### **D6.3 Simulation support for WP1 experiments: Overview of results**

One of the main tasks of WP2 is to provide “support in terms of simulation models for the experimental optimization study envisaged in WP1”. In order to do so, WP2 partners performed virtual experiments with the aim to point out the features and the novelty of the NEWS techniques (major topic in D6). For each of the WP1 experiments listed below, one or more WP2 groups have developed a numerical simulation support. The synthesis of the relevant results (and a comparison with experimental data, wherever possible) are included in this report:

- (a) Phase modulation: GIP-U (experiments: GIP-U)
- (b) Nonlinear reverberation: KULeuven
- (c) Nonlinear Rayleigh wave propagation: KULeuven
- (d) Frequency modulation: GIP-U, CU (experiments: CU)
- (e) Longitudinal resonance: POLITO
- (f) Bispectral analysis: UNIVBRIS

In the following descriptions most simulations have been kept simple and are performed for one-dimensional (1D) cases. It should be noted that each numerical experiment can equally well be reproduced in 2D or 3D. Besides, it is also possible to perform the simulations in different pre-stress conditions.

**(3a) Phase modulation**

This method to measure in contact the nonlinearity parameter  $\beta$  (“classical” nonlinearity) of solid plates has been used in experiments conducted in WP1. In this method, a high frequency (HF) tone-burst signal of 15 MHz is inserted in the material by a contact-transducer (with a suitable coupling). A low frequency (LF) pulse (1.5 MHz) is applied to the other face, in the opposite direction, such that the nonlinear interaction of the two waves takes place during the back propagation toward the HF transducer (Figure 3a.1 (a)). This collinear interaction creates a phase modulation of the HF tone-burst which is directly proportional to the  $\beta$  coefficient and the particle velocity of the LF wave. To determine this particle velocity a self reciprocity calibration of the contact LF transducer is used. A numeric phase demodulation is then performed, giving the beta coefficient of the sample (Figure 3a.1 (b)).

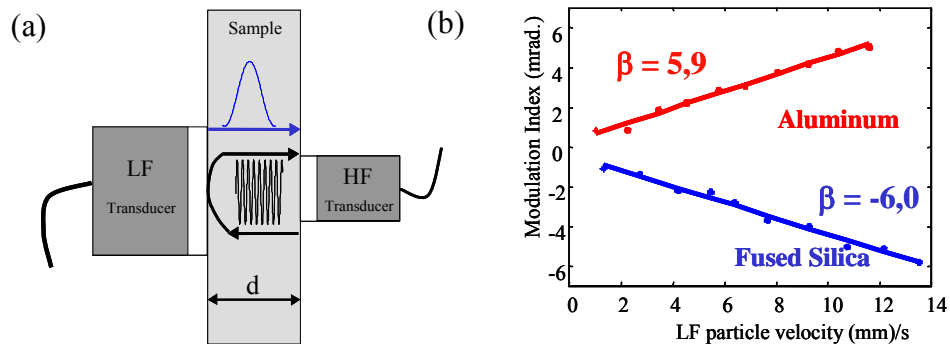


Figure 3a.1: (a) Principle, and (b) experimental results obtained with the phase modulation method.

In the case of hysteretic nonlinearity (with the nonlinear parameter  $\gamma$ ) the induced phase modulation by the interaction of a low frequency pulse and a high frequency tone-burst is difficult to predict analytically. So, 1D simulations of this nonlinear process have been made with the pseudo-spectral solver in the case of rectangular HEUs (Figure 2.a.2 (a)). The simulated sample is a 1 cm thick aluminium plate and the HF wave is a 400 periods tone-burst. First, the sample is considered as a homogeneous “classical” nonlinear solid, in order to validate the pseudo-spectral solver used. The obtained simulated results (Figure 3a.2 (a)) compare favourably with experiments, and it is shown that the time evolution of the phase modulation is similar to the LF particle velocity as predicted by analytical calculations.

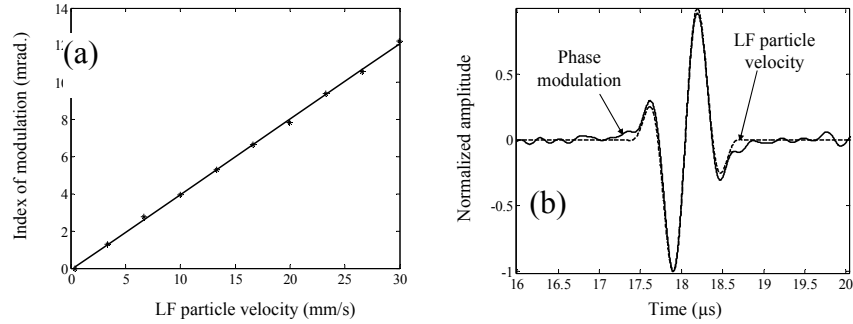


Figure 3a.2: (a) Index of modulation as a function of LF particle velocity, and (b) comparison of LF particle velocity and phase modulation time evolutions in a “classical” nonlinear solid.

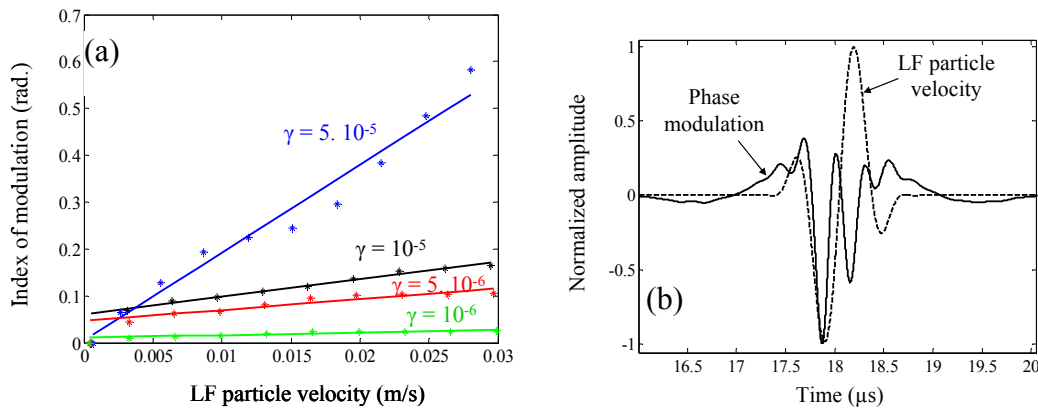


Figure 3a.3: (a) Index of modulation as a function of LF particle velocity, and (b) comparison of LF particle velocity and phase modulation time evolutions in a nonlinear hysteretic solid.

Now, as shown in Figure 3a. 3(b), the time evolution of the induced phase modulation, in homogeneous nonlinear hysteretic solids, is no more a replicate of the LF particle velocity. The mean frequency of the phase modulation is here to time the one of the LF pulse. Nevertheless, a linear increase of the index of modulation as a function of the nonlinear parameter  $\gamma$  can be seen in Figure 3a. 3(a) in the high amplitude LF particle velocity range. To obtain the same amplitude of modulation index as the one measured in the aluminium sample, a nonlinear parameter  $\gamma$  of only  $5 \cdot 10^{-7}$  is needed. So, the phase modulation can be used to measure the hysteretic nonlinear parameter of homogeneous sample.

The main purpose of the project is to determine if a NEWS method is able to locate a defect (a nonlinear hysteretic zone) inside a linear sample. So, simulations have been made for a linear and homogeneous sample with a small (150 μm) nonlinear hysteretic zone. The obtained simulated results (Figure 3a.4) show that the phase modulation method is not able to locate the defect, if only one emitter and one receiver are used. The method is only able to tell us if a defect is located between the two transducers. So, in order to make a localization of defects, a large number of transducers, and a tomography algorithm need to be used.

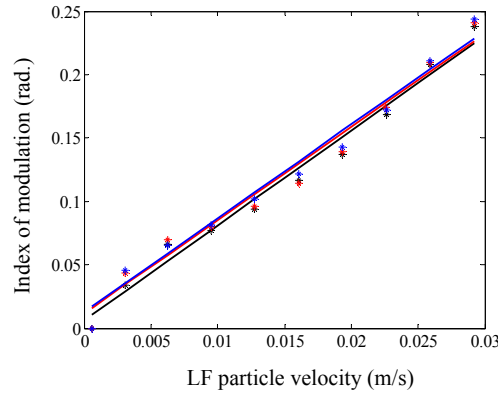


Figure 3a.4: Comparison of the index of modulation vs LF particle velocity for 3 positions of a 150 $\mu$ m defect in a 1 cm thick homogeneous and linear sample.

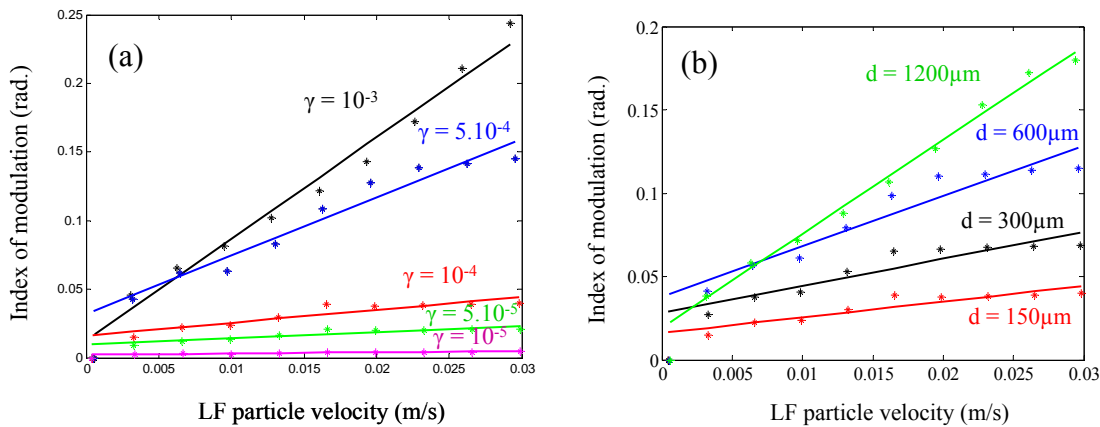


Figure 3a.5: Effect of (a) the nonlinear hysteretic parameter, and of (b) the defect size  $d$  on the Index of modulation vs LF particle velocity curves.

Finally, it can be seen in Figure 3a.5 that the effects of an increase of the nonlinear parameter or of the defect size are similar. In both cases a linear increase of the measured index of modulation is predicted. So, the size or the nonlinear hysteretic parameter  $\gamma$  of the defect zone can not be determined separately. The phase modulation method is only sensitive to the product of the two parameters.

According to the limits of the contact phase modulation method, new techniques have been developed in order to detect micro-damage (WP2.2).

### (3b) Nonlinear reverberation

The presence of nonlinear and hysteretic features (i.e. microdamage) can be observed from a careful analysis of the reverberation of a response signal after a finite interval CW excitation with a frequency near the frequency of resonance. This method has been used in experiments conducted in WP1 on thermally exposed CFRP samples at different temperatures (240°C-300°C) and different exposure times (15' to 60'). A typical response signal is shown in the figure below (figure 3b.1). The reverberation signal can be analysed as function of time using short time windows and fitting routines with exponentially decreasing sine functions. The fitting parameters allow us to produce a parametric plot of frequency versus amplitude. From the frequency reduction with amplitude one can determine the degree of nonlinearity and relate this to the extent of damage in the material.

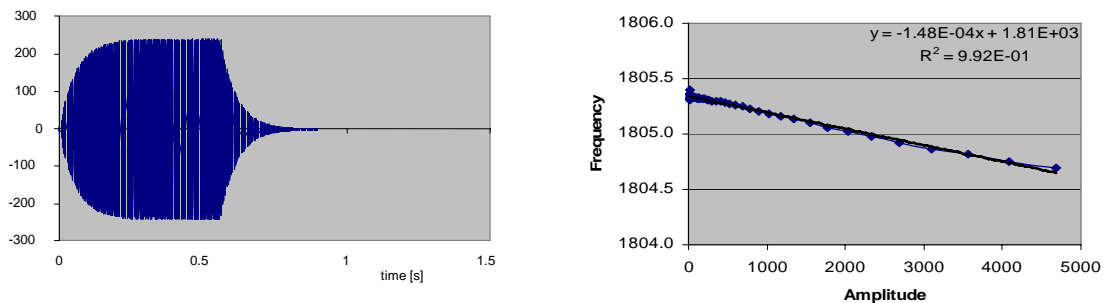


Figure 3b.1: Experimental procedure and analysis results for nonlinear reverberation experiments on thermally damaged CFRP samples

To simulate this effect and quantify the nonlinearity in relation to the actual damage in the material, we have used a finite difference implementation of the Euler-Bernoulli beam equation with inclusion of hysteretic nonlinearity and linear damping. The linear parameters are taken from the experiment, so that linear resonance frequency and linear attenuation matches the data. The nonlinearity (only non-classical) is globally distributed over the sample (no localization). The comparison of the results for an exposure to 300°C and 60' is shown in figure 3b.2. The simulations track the experimentally observed resonance frequency reduction extremely well. For the nonlinearity in the damping, the experimental data are noisier, but the tendency predicted in the simulations is more or less the same.

It is worth noting that the nonlinear contribution which has to be used in the numerical model is quite small. For the largest effects measured in the experiments, we are using a value of  $\gamma \approx 2 \cdot 10^{-19}$  (this is the deformation contribution of one single hysteretic element). If we assume a constant density in the statistical PM-space, ranging from -5MPa to 5MPa, this would amount to a hysteretic contribution to the strain of only  $\gamma N \approx 10^{-5}$ .

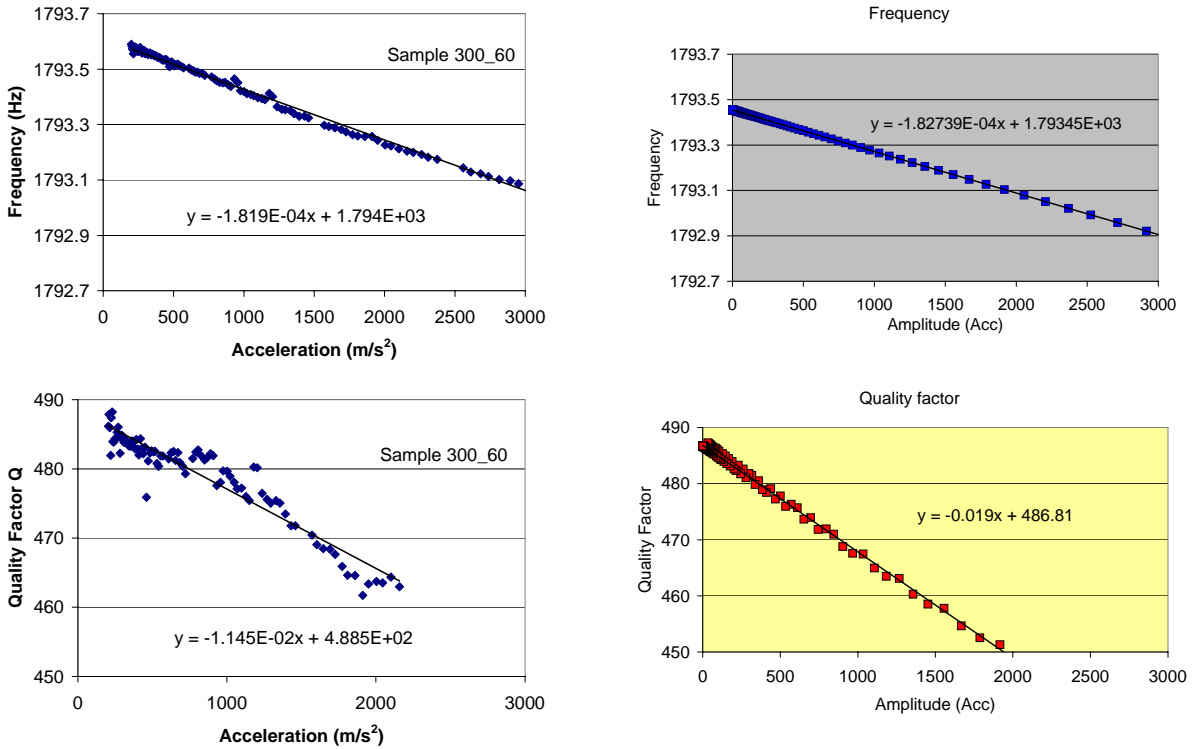


Figure 3b.2: Experimental (left) and simulations (right) for nonlinear reverberation: analysis of the resonance frequency reduction (top) and the amplitude dependence of the quality factor (CFRP sample 300°C for 60').

The numerical values of the nonlinearity deduced from the best fits of the analysed experimental data are shown below as function of the exposure time and temperature. These values will be compared to an analysis of thin sections of these samples in the near future to quantify the nonlinearity in relation to density of microcracks, etc.

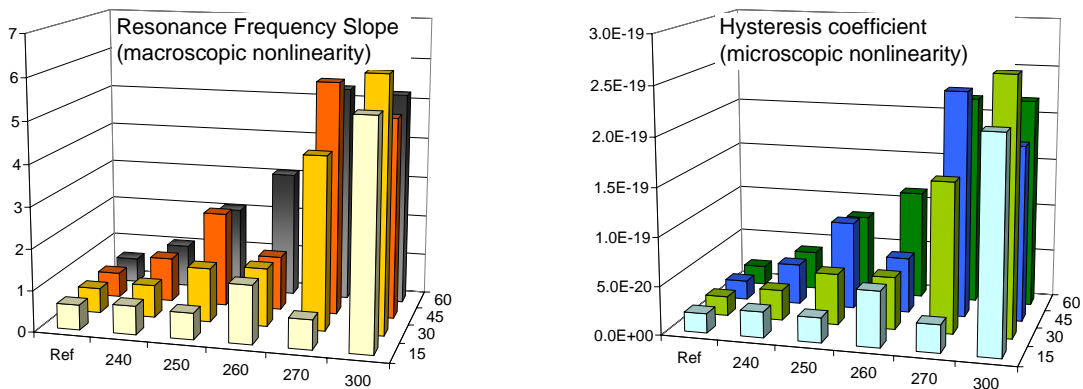


Figure 3b.3: Experimental (left) and simulations (right) of the nonlinearity in thermally damaged CFRP samples as function of temperature and exposure time.

### (3c) Nonlinear Rayleigh wave propagation

In this paragraph we illustrate the multiscale model for a 2D simulation of nonlinear Rayleigh Wave Propagation. The outcome of the simulations is interesting for tuning the actual experiments considering Rayleigh waves in WP1. The model can be easily extended to the propagation of Lamb waves.

We consider a solid medium measuring  $120 \times 50$  mm<sup>2</sup>, with a density of  $1000$  kg/m<sup>3</sup>, an overall longitudinal velocity of  $2000$  m/s, and a shear velocity of  $1155$  m/s. No linear attenuation mechanism is assumed within the body. The top side of the medium is considered to be free (air). The solid body (SB) is surrounded by three absorbing boundary layers (left, right and bottom) to avoid artificial reflections from the numerical boundaries. The source  $S$  is located on the free surface, at the left hand upper corner of the solid body. Two receivers  $R_1$  and  $R_2$  are located at  $20$  mm and  $100$  mm from the source (see Figure 3c.1). A surface zone (Zone), centred at  $60$  mm from the source, is considered to be microdamaged. Everywhere else the solid body is linear elastic ( $\lambda_{SB}=1.332$  GPa,  $\mu_{SB}=1.334$  GPa, and  $\gamma_{SB}=0$ ).

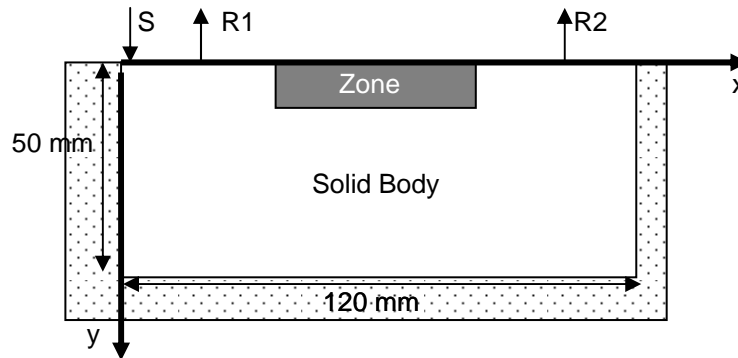


Figure 3c.1: c Rayleigh wave propagation simulation

The excitation signal is modelled as an apodized sinusoidal force  $F_y$  with frequencies ranging from  $50$  to  $200$  kHz, and is treated as a local source term for the  $v_y$  component in at position  $S$  on the free surface.

Experimental work on progressively damaged materials has shown that microdamage can result in a reduction of the linear moduli on one hand, and/or an increase of the nonlinearity on the other hand. We have investigated these effects in the model simulations by considering various cases with gradually varying linear and nonlinear hysteretic parameters in the “microdamaged” zone near the surface. In order to avoid reflections from discontinuous transitions in parameters between layers, we assume generalized Gaussian distributions for the shear modulus  $\mu$  and of the hysteresis parameter  $\gamma$  in the following form

$$\mu(x, y) = \mu_{SB} \left( 1 - \mu_R e^{-\frac{1}{P} \left[ \frac{x-x_s}{W_x} \right]^P - \left[ \frac{y-y_s}{W_y} \right]^2} \right), \quad \gamma(x, y) = \gamma_{MAX} e^{-\frac{1}{P} \left[ \frac{x-x_s}{W_x} \right]^P - \left[ \frac{y-y_s}{W_y} \right]^2}$$

For the calculations, we considered distributions of  $\mu$  and  $\gamma$  which are centered in the  $x$ -direction at  $60$  mm from the source ( $x_s=60$  mm) with a width equal to  $W_x=12$  mm, and centred in  $y$ -direction at the surface ( $y_s=0$ ) with variable width  $W_y$ . The parameter  $P$  was

set to 8. The maximum reduction of the modulus in the damaged zone (at the surface) is 20% ( $\mu_R=0.2$ ). The maximum strength of the hysteretic nonlinearity at the surface corresponds to  $\gamma_{MAX}=2 \cdot 10^{-18}$ . The stress-strain relation of the material cells in the damaged zone is updated in the assumption of a uniform PM-distribution and only volumetric hysteresis is considered. No classical nonlinearity is assumed.

We investigate the influence of hysteresis and/or modulus reduction in two ways. First, we examined the effect on the phase velocity of the Rayleigh wave component along the surface. To do this we considered 6 cases: Case 1 = Linear Defect, Case 2 = Defect with Uniform Hysteresis, Case 3 = Defect with Layered Hysteresis, Case 4 = Linear Defect with Modulus reduction, Case 5 = Defect with Uniform Hysteresis and with Modulus reduction, Case 6 = Defect with Layered Hysteresis and with Modulus reduction. We determined the phase velocity for these six cases at different excitation frequencies ( $f$ ) from the difference of the phase spectra at  $R_1$  and  $R_2$  following the method described in seismology [Aki and Richards]. This procedure was repeated for various cases with and without modulus reduction, and with and without hysteresis.

The results of this investigation led to the following twofold conclusion (illustrated in Figure 3c.2 for different depths of the defect zone): A) The wave speed of a Rayleigh wave is highly dependent on the stiffness of the near-surface layers, and a modulus gradient introduces dispersion or frequency dependent wave speeds. This is well-known in seismology and NDT as linear depth profiling, and is attributed to the difference in penetration depth of the Rayleigh wave at different frequencies. B) The (microscopic) nonlinearity has little or no “measurable” EXTRA effect on the wave speed of a propagating Rayleigh wave. This latter observation can also be readily explained by recalling that the nonlinearity is a second order effect on the modulus reduction which is typically below 0.1%. The effect on the Rayleigh wave velocity is thus minimal, and extremely hard to measure in situ.

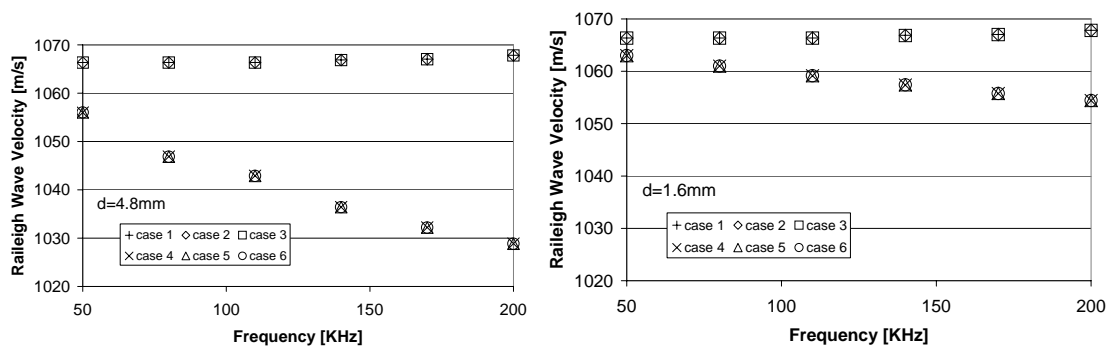


Figure 3c.2: Rayleigh wave simulations in a nonlinear (microcracked) medium. Frequency dependence of the Rayleigh wave velocity for different depths of the microdamaged zone ( $d=4.8$  and  $1.6\text{mm}$ ).

In the second set of simulations, we concentrate on the nonlinear properties of Rayleigh wave propagation by analyzing the level of the third harmonic spectral component of the Rayleigh wave's out of plane particle velocity  $v_y$  along the surface. It is well known that the third harmonic in a one-dimensional hysteretic nonlinear bar (in the absence of attenuation) accumulates linearly with distance, and is quadratic in the amplitude of the fundamental component. We have found the same dependencies for the out of plane particle velocity of

the Rayleigh wave (not shown for brevity) propagating along the surface in 2D. With regard to the frequency dependence, the displacement amplitude  $u_{3f}$  is generally quadratic in the driving frequency. Taking into account the extra frequency dependence for velocity components (“ $v = \omega u$ ”), we may expect a cubic frequency dependence for the third harmonic particle velocity  $v_{y,3f}$  at a fixed position and for a fixed excitation level.

In Figure 3c.3a, we compare the results of layered hysteresis without modulus reduction for different depth of the microdamage region (by assuming different parameters for the width  $W_y$ ). The results first of all show the predicted cubic relationship with frequency. As can be expected, we observe that the 3rd harmonic component diminishes with decreasing depth of the microdamaged zone. However, Figure 3c.3b (a normalized version of Figure 3c.3a) clearly illustrates that the reduction is highly frequency dependent. Compared to the value at  $W_y = 2.5\text{mm}$ , the 3rd harmonic for  $W_y = 0.2\text{mm}$  reduced by more than 80% at 50 kHz and only by 45% at 200kHz. This is again an expected result which is related to the frequency dependent penetration depth of Rayleigh waves.

This yields a second conclusion: the amplitude of the 3rd harmonic of a Rayleigh wave is highly sensitive to the microscopic nonlinearity of the near-surface layers and a nonlinearity gradient introduces a new type of dispersion on the harmonics.

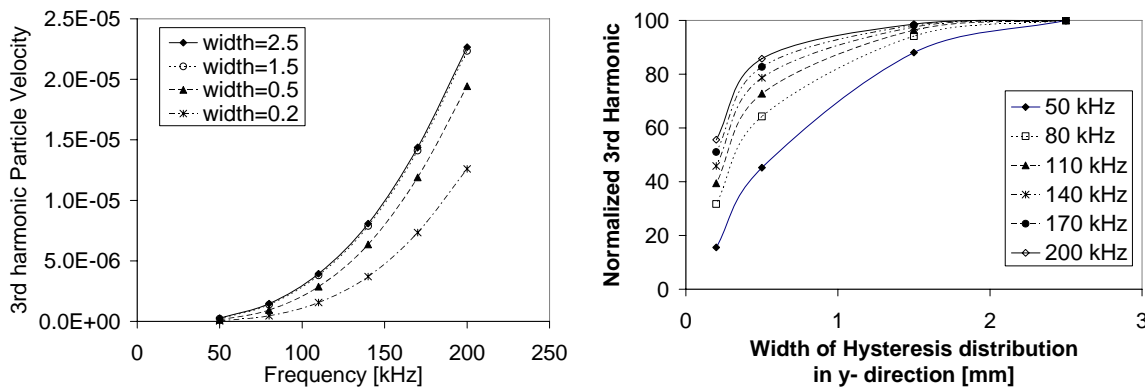
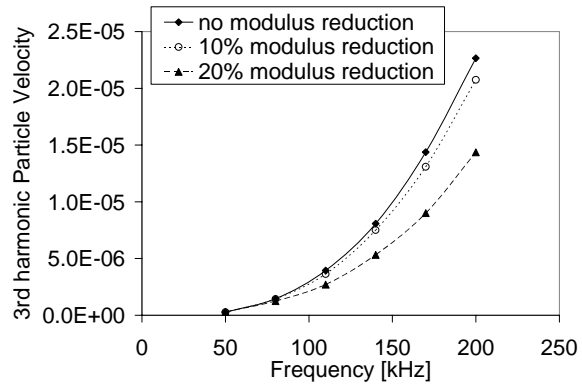


Figure 3c.3: Rayleigh wave simulations in a nonlinear (microcracked) medium

- Frequency dependence of the 3rd harmonic particle velocity component  $v_y$  in the Rayleigh wave propagation for different depths of the microdamaged zone without modulus reduction.
- same results as in figure 3c.3a, but plotted in normalized form as function of the depth.
- Frequency dependence of the 3rd harmonic particle velocity component  $v_y$  in the Rayleigh wave propagation for different levels of modulus reduction.



*Figure 3c.4: Rayleigh wave simulations in a nonlinear (microcracked) medium. Frequency dependence of the 3rd harmonic particle velocity component  $v_{y,3f}$  in the Rayleigh wave propagation for different levels of modulus reduction.*

Finally we considered a modulus reduction on top of a hysteretic nonlinearity. Figure 3c.4 illustrates the frequency dependence of  $v_{y,3f}$  at  $R_2$  for a zone with given hysteretic nonlinearity and different levels of modulus reduction. A reduction of the modulus in the microdamaged zone leads to a reduction in the observation of the 3rd harmonic of the particle velocity  $v_y$  too.

These results are extremely encouraging for the use of depth profiling methods based on the analysis of the generated harmonic content as function of frequency.

### (3d) Nonlinear frequency modulation

One of the most critical damage experienced by aircraft industry is the barely visible impact damage and its early detection is one of the priorities of aircraft industries. At this aim and to give “support in terms of simulation models for the experimental optimisation study envisaged in WP1”, it was decided to perform a virtual experiment with the aim to point out the capability of a NEWS techniques in detecting this type of damage and to understand the effect of impact damage on the nonlinear elastic behaviour of impacted aircraft structures. A frequency modulation numerical experiment was performed on a 2D laminate structure. The panel was made of eight layers with the following ply orientation  $[0/90]_4$ . Lamina thickness is 1.5mm with the following material properties:

$$E_{11}=144.8\text{GPa}; E_{22}=9.7\text{GPa} ; E_{33}=9.7\text{GPa} ; G_{12}=6\text{GPa} ; G_{23}=3.6\text{GPa} ; G_{13}=6\text{GPa} \\ \nu_{12}=0.3; \nu_{23}=0.34 ; \nu_{13}=0.3; \rho=1600 \text{ kg/m}^3.$$

Two damage locations and length (0.005/0.01m) were considered as shown in Figure 3d.1. Damage was considered to affect 4 inside layers. This damage represents a typical damage caused by a low velocity impact. The impact damage was simulated by a hysteretic nonlinear material represented by a uniform density PM-space elements in the triangle (-5MPa, 5 MPa). The contribution to the strain when all elements are closed equals  $20^{-3}$ . A bi-tone excitation was used with the following frequencies:  $f_1=10\text{kHz}$ ,  $f_2=150\text{kHz}$  and with the following amplitudes  $A_{f1} = 2.5 \text{ MPa}$ ,  $A_{f2} = 1\text{MPa}$ .

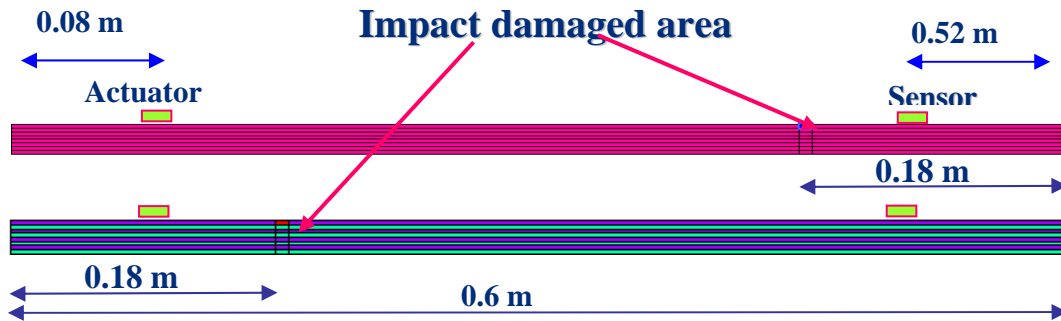


Figure 3d.1 - Experimental setup.

The results showed that the damage introduced odd harmonics of the low frequency and odd sidebands of the high frequency excitation as shown in the following figures. No harmonics of the high frequency excitation were observed. The results showed that harmonics and sidebands were recorded only on the PM-space signal spectrum highlighting the capability of the current constitutive model was able to describe the barely visible impact damage and to provide support for the optimisation of the experimental activity in WP1.

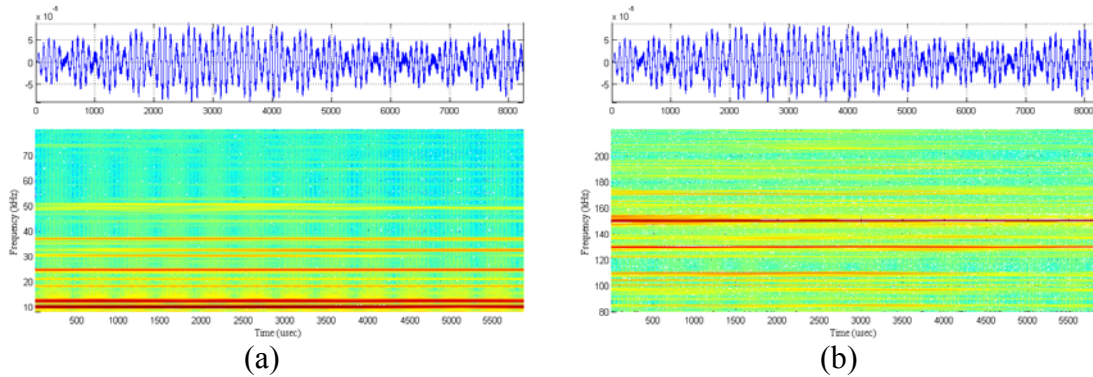


Figure 3d.2 – a) Harmonics of  $f_1$  (10kHz), b) Sidebands

### (3e) Longitudinal (in plane) resonance simulations

In this section we show how nonclassical nonlinear defects influence the value of the resonance frequency for in plane longitudinal vibrations. The degree of resonance frequency reduction as function of the deformation can be used as a sensitive damage indicator. With this aim we performed 1D virtual experiments on a thin bar, changing subsequently the intensity of the damage, its position and width.

A longitudinal resonance experiment is generally performed as follows: a rod-shaped specimen (of length  $L$ ) is suspended in its centre and is equipped with a transducer generating monochromatic waves of variable angular frequency. The response signal is recorded at the other end by means of a receiver. The angular frequency of the forcing is swept around the longitudinal resonance mode(s) of the specimen and the amplitude of the output strain (or the average output velocity) is recorded after transient phenomena have disappeared. The experiment is performed several times for increasing amplitudes of the excitation.

In the simulations, we assume free boundary conditions at both edges of the sample. At the left boundary we assume a known applied sinusoidal forcing with given frequency and amplitude. The damage is modelled by a hysteretic nonlinearity and is localised at position  $x_c$  and has a width  $w$ . Simulations are performed for discrete frequency steps and increasing input excitation amplitudes.

The simulated resonance curves (averaged output velocity vs. frequency) are reported in Figure 3e.1a for increasing values of the amplitude of the excitation; the center of the nonlinear defect is placed in  $x_c = L/2$  and its width  $w = L/20$ . In agreement with experimental results (for instance on thermally damaged CFRP samples), the resonance frequency  $\omega_r$  (i.e. the frequency at which a maximum in the response is obtained) is shifted downwards for increasing driving amplitudes. In Figure 3e.1b we reported the value of the resonance frequency versus the input amplitude, and in Figure 3e.1c its relative variation with respect to the frequency at zero input amplitude. The degree of resonance frequency reduction strongly depends on the features of the defect (intensity, position and length).

If we increase the damage intensity (or equivalently decrease  $\alpha$ , as described in the section 6.2 about the model used by POLITO), the corresponding macroscopically observable nonlinear effects increase as well. Indeed, for an identical simulation ranging over the same driving amplitudes, the shift of the resonance frequency is much higher for  $\alpha = 0.47$  than

for  $\alpha = 0.49$  (where  $\alpha = 0.5$  represents an intact sample), see Figure 3e.2. We also note, that the resonance frequency in the limit of an extremely small driving amplitude (from now on called linear resonance frequency,  $\omega_0$ ) varies when changing the value of the level of damage/nonlinearity ( $\alpha$ ). This reflects the linear modulus reduction due to the presence of damage. However, it is clear that the nonlinear signature is more sensitive than the linear one.

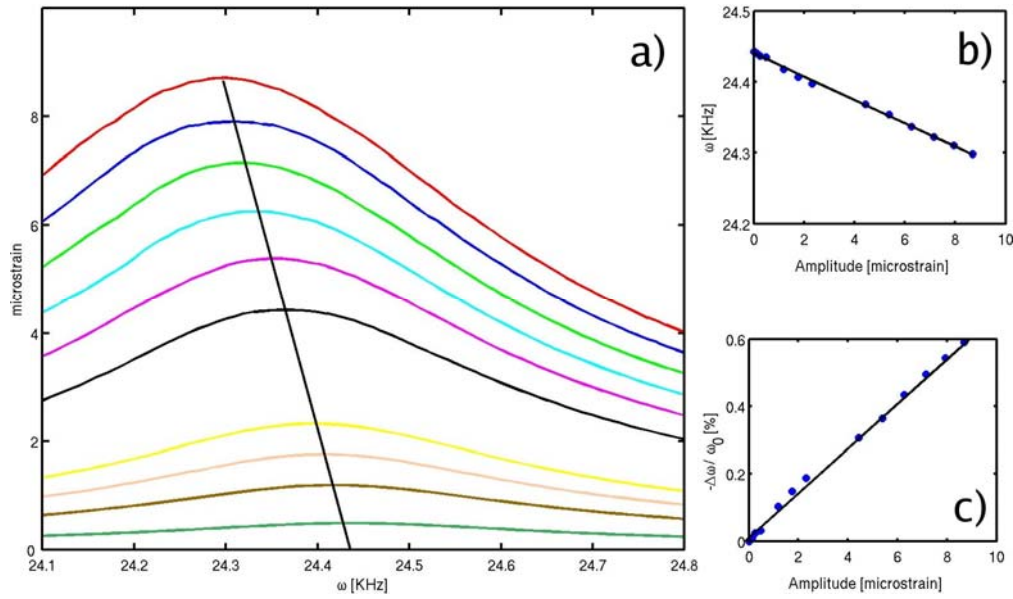


Figure 3e.1: Resonance frequency shift as function of response amplitude

Other interesting effects on the resonance frequency shift can be obtained by varying the defect position ( $x_c$ ). As expected, the nonlinear effects depend on the defect location and are much larger when the defect is localised in the centre of the bar, where strains of the first natural frequency are largest: Figure 3e.3a-b shows that the frequency shift increases up to 0.6% when  $x_c = L/2$ , while it is only 0.2% for  $x_c = L/4$ . This is an interesting result in view of imaging methodologies, and can be used in the identification of the location of damage (see deliverable D7, MuMoNRAS).

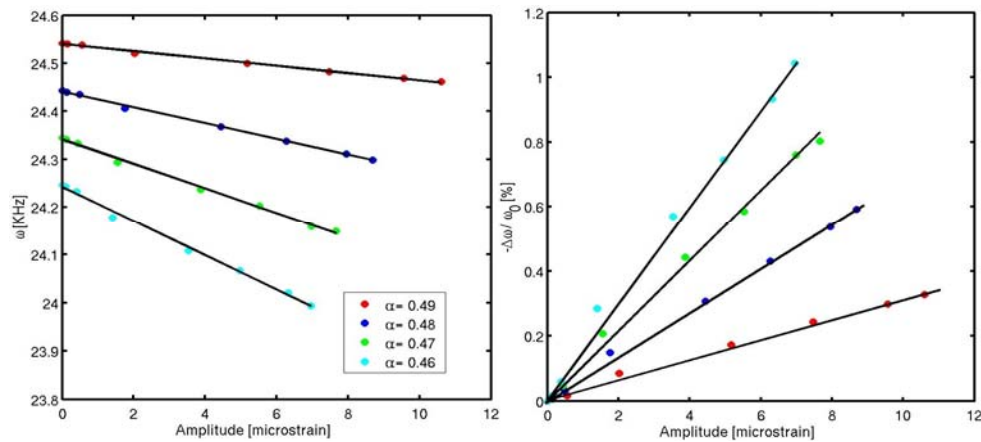


Figure 3e.2: Shift of the resonance frequency for various damage levels

Finally, in Figures 3e.3c-d, we analyse effects due to changes in the damage size. As expected, the effects on  $\omega_0$  and on the slope of the resonance frequency reduction are more evident when the size of the damaged zone increases.

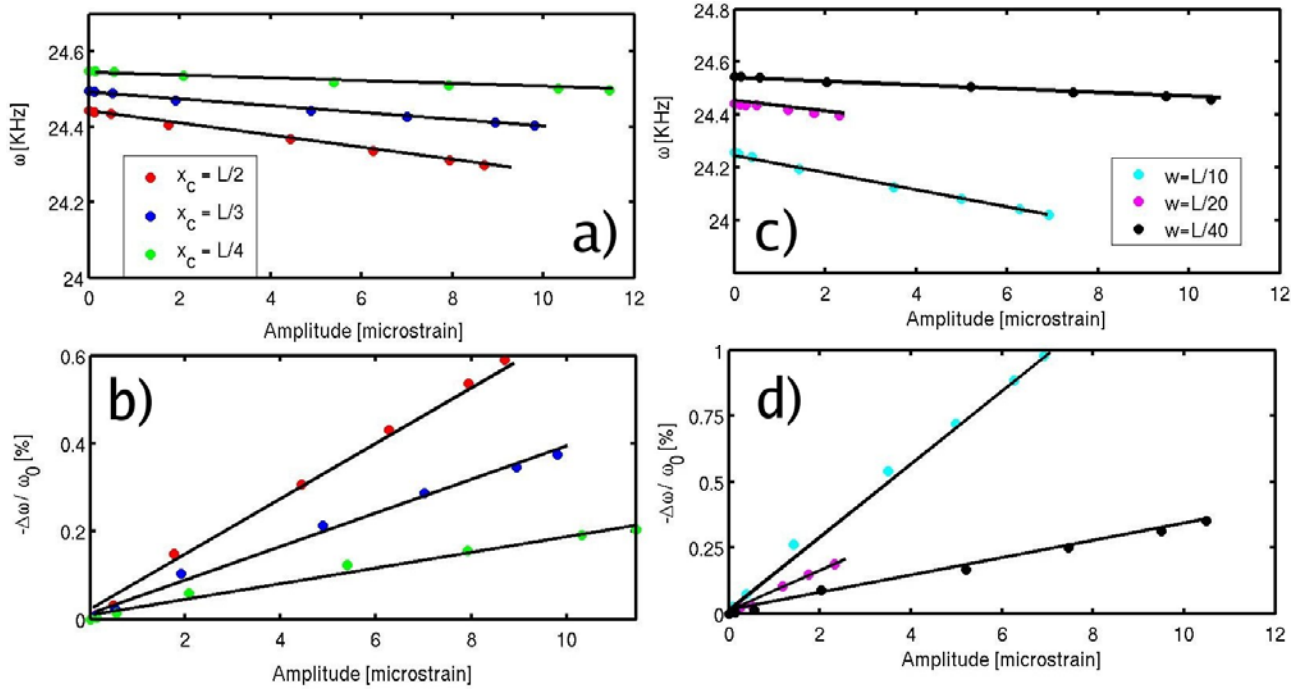


Figure 3e.3: Shift of the resonance frequency for various locations of a localised zone of microdamage (right), and for various widths of the localised zone (left).

**(3f) Bispectral analysis and ultrasonic intermodulation**

At the University of Bristol a ultrasonic modulation technique using bispectral analysis is being developed and applied to extended structures (as part of WP 1). The modelling work undertaken in WP2 is in support of this. The experimental system applies two ultrasound signals (100–500kHz) to a sample and detects the signal resulting from the behaviour of the sample. Non-linearity, such as that due to a fatigue, results in the mixing of the two applied signals and by detecting the signal due to mixing the degree of non-linearity is determined. Bispectral analysis is used to detect the mixing frequencies in the signal.

It is common in signal processing, when analysing a signal  $x(t)$  with Fourier transform  $X(f)$ , to calculate second moment, or the power spectrum:

$$P(f) = E[X(f)X^*(f)]. \quad [3g.1]$$

Where  $E[\ ]$  is the expectation value operator.

The bispectrum is the third moment of  $X(f)$ :

$$B(f_1, f_2) = E[X(f_1)X(f_2)X^*(f_1+f_2)]. \quad [3g.1]$$

For a given pair of frequencies  $f_1, f_2$  there are four conditions for the bispectrum to be non-zero:

- 1)  $X(f_1) \neq 0$
- 2)  $X(f_2) \neq 0$
- 3)  $X(f_3 = f_1+f_2) \neq 0$
- 4)  $\phi_3 = \phi_1 + \phi_2$  (The three signals in conditions 1, 2 and 3 are quadratically phase coupled).

*The Results:* Parameters were chosen to give behaviour similar to that of our real system:

<b>Model Parameters</b>	
Excitation frequency 1, $f_1$	200 kHz
Excitation frequency 2, $f_2$	350 kHz
Closed spring stiffness, $K_0$	1 Nm <sup>-1</sup>
Stiffness reduction, $\Delta K$	0.1 Nm <sup>-1</sup>
Total time, $T$	0.1s
Time Step, $dt$	$2 \times 10^{-7}$ s
Input Amplitude, $A_0$	1

The resulting bispectrum shows the same features as experimental data:

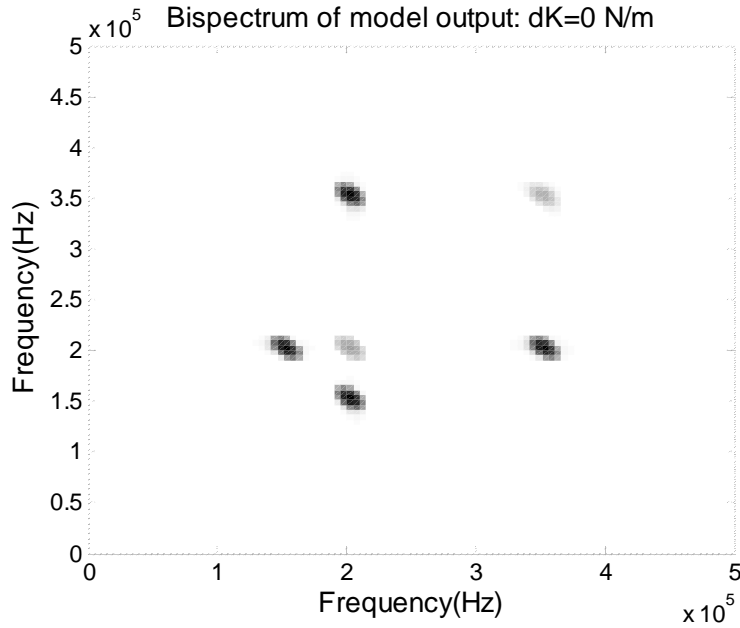


Figure 3f.1: Bispectrum of bilinear model ( $\Delta K = 0.1$ ) response to excitation at 200kHz and 350kHz.

Note that some smoothing of the peaks has been introduced to improve their visibility.

Away from the diagonal, where the peaks correspond to one signal interacting with its harmonic, peaks only occur where there are signals at three different frequencies. As the system is excited only at two frequencies any off diagonal peak must correspond to interaction with a signal due to the non-linear behaviour of the system, running the model without noise and with  $\Delta K = 0 \text{ Nm}^{-1}$  (a linear system) leads to a bispectrum plot with no values above 0.3% of the non-linear system's bispectrum peaks. In experimentally characterising our samples' non-linearity the peak  $B(F_1, F_2 - F_1)$ , resulting from the two input signals plus the difference signal produced in the sample. Figure 3f.2 shows how this peak behaves in the model as  $A_0$  increases we see that  $B^{1/3}(F_1, F_2 - F_1) \propto A_0$ :

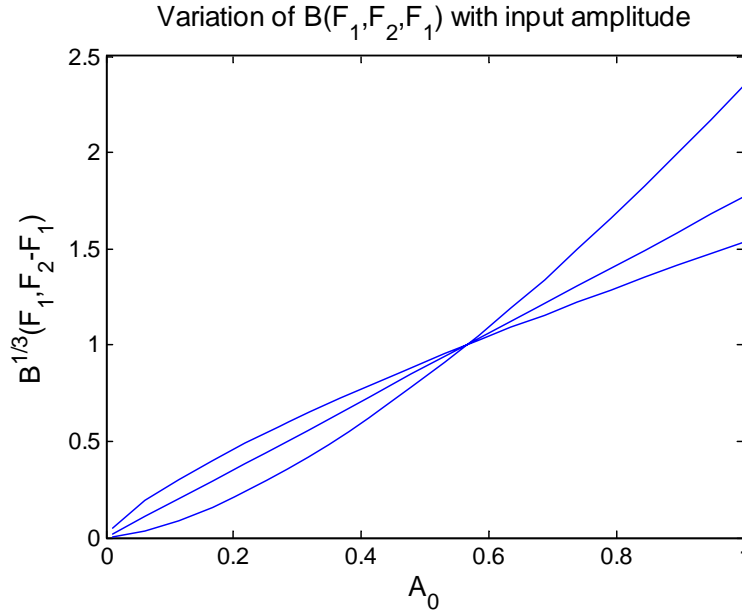


Figure 3f.2: Variation of bispectral response with increasing excitation amplitude for bilinear system.

Also plotted (dashed lines) are  $B^{1/2}(F_1, F_2 - F_1)$  and  $B^{1/4}(F_1, F_2 - F_1)$  for comparison. Also of interest has been the behaviour of the peak with respect to increased non-linearity shown in figure 3f.3.

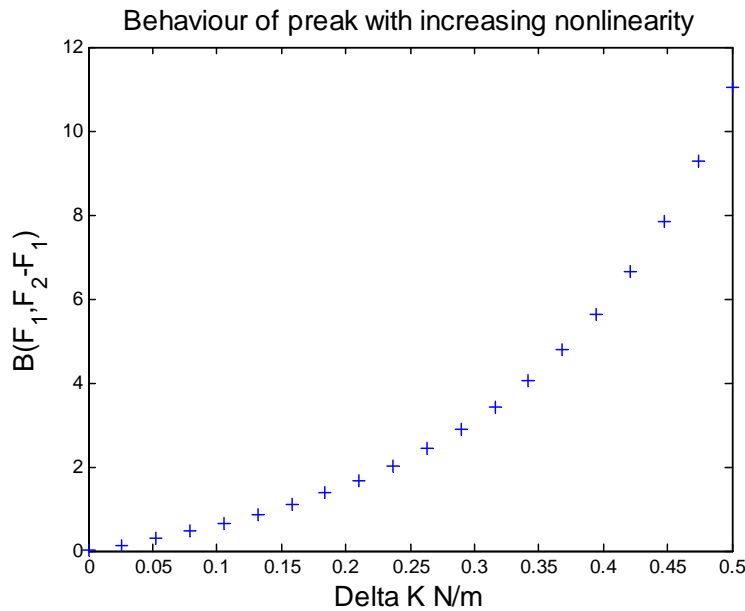


Figure 3f.3: Variation of bispectral response with increasing non-linearity.

Despite its apparent simplicity the bilinear spring model gives insights into the behaviour of the bispectrum signal corresponding to nonlinear systems excited by a pair of ultrasound signals, as used in the ultrasonic modulation technique. It also provided a useful test bed

when considering the best parameters and data acquisition to use in the bispectral analysis of experimental data.

It became clear experimentally (during tests on 60mm × 60mm × 400mm steel blocks as part of WP1) that, not only were resonances of the experimental samples close together in the frequency regime, but that the exact mode selected strongly affected the response for a given sample and damage state. FE models of the block gave an idea of the highly complex modal structures at high frequencies for even these simple samples, helping to explain the apparently random relationship between frequency of excitation and the level of non-linearity in a damaged sample.

A smaller cross-section sample was designed with the aim of reducing the complexity of the modes involved and so easing analysis of experimental data and modelling. The new samples were 88mm long with a cross section of 5mm by 6.35mm and a 1mm notch at the mid point to initiate fatigue cracking. Experimentally the sample was instrumented with 5mm-diameter 2mm-thick piezoceramic disks, one at each end for excitation and detection of the 100kHz-500kHz ultrasound signals. Figure 3f.4 shows all the modes evaluated using a 3D FE model. There are far more modes than were detected experimentally (by exciting the sample with a swept signal and observing local maxima in the response). The nature of the excitation and detection was thought to be the cause of this discrepancy and so modes in the model where the motion of all nodes at the ends of the sample is in phase were identified. These are the modes circled red in figure 3f.4, the nodal displacements for some of these modes are shown in figure 3f.5.

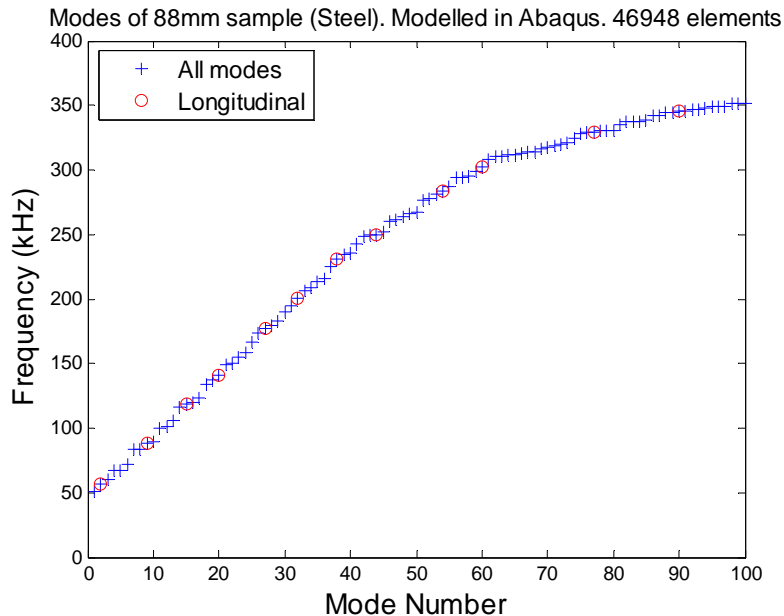


Figure 3f.4: Frequencies of high order resonances of 88mm × 5 mm × 6.35 mm steel sample calculated using 46948 element 3D FE model.

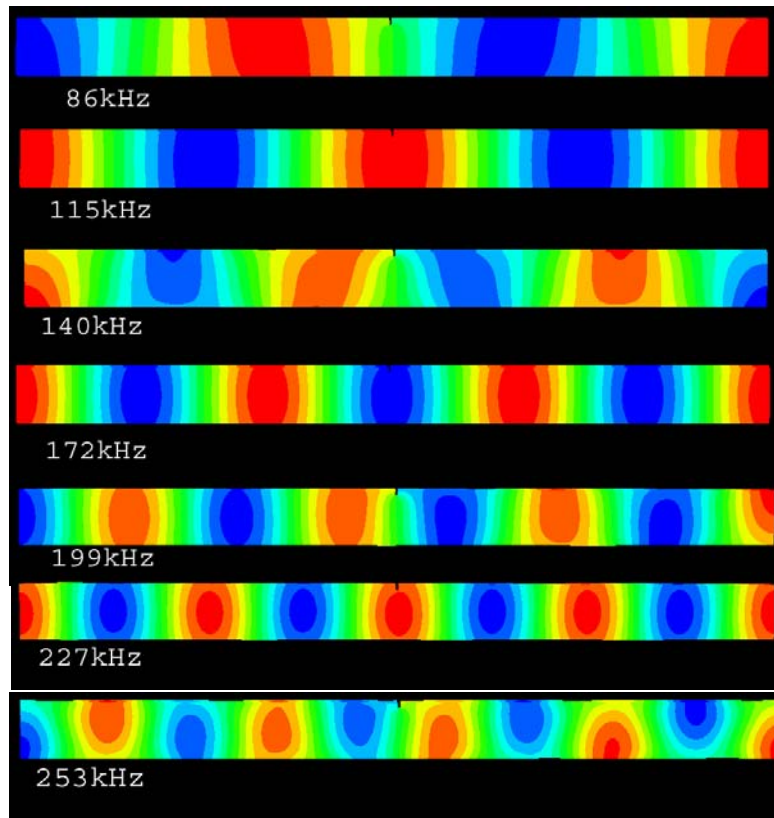


Figure 3f.5. Colormaps of the longitudinal displacement of the sample from FE model. Red is maximum positive (along axis of sample) displacement to left and blue negative.

Figure 3f.6 shows a comparison of the frequencies of these ‘longitudinal’ modes with those obtained experimentally. Although there is some difference in frequencies the qualitative behaviour and the mode separation is in good agreement. The apparently straightforward nature of the modes excited suggested that a simple 1D model could produce a useful representation, whilst being computationally less demanding, and important consideration when more complex calculations relating to non-linear behaviour are to be considered. A one-dimensional FE model of the system was developed in Matlab and its modes calculated, these are shown in figure 3f.6. Again, there is good qualitative agreement with the experiment and the 3D model. Having produced a simple model of the experimental system attempts were made to introduce non-linearity: experimentally this was achieved by fatiguing the sample until a crack developed at the mid-point notch and in the one-dimensional model by introducing bilinear behaviour to one element (corresponding in position to the notch). Two approaches to measuring the non-linearity, measuring the intermodulation of two exciting frequencies and measuring the harmonics generated if a single excitation frequency was applied. In the model the excitation was modelled as a force applied to the node at one end of the sample. The 4<sup>th</sup> order Runge-Kutta method was used to solve for the evolution of the system and the motion of the end node (opposite to the input) used as the ‘measured’ signal. Unfortunately neither experimentally nor in the model could significant degrees of non-linearity be detected. Two hypotheses were suggested for this difficulty: one that, experimentally, the fatigue crack had bent open due

to the narrow nature of the samples and so acted linearly and the second that the simple modal structure resulted in the excited modes dominating the response with little or no response at other frequencies. The fact that neither the experiment nor the model demonstrated non-linearity suggested that it was the later problem, but sufficient work has not been completed to show this conclusively.

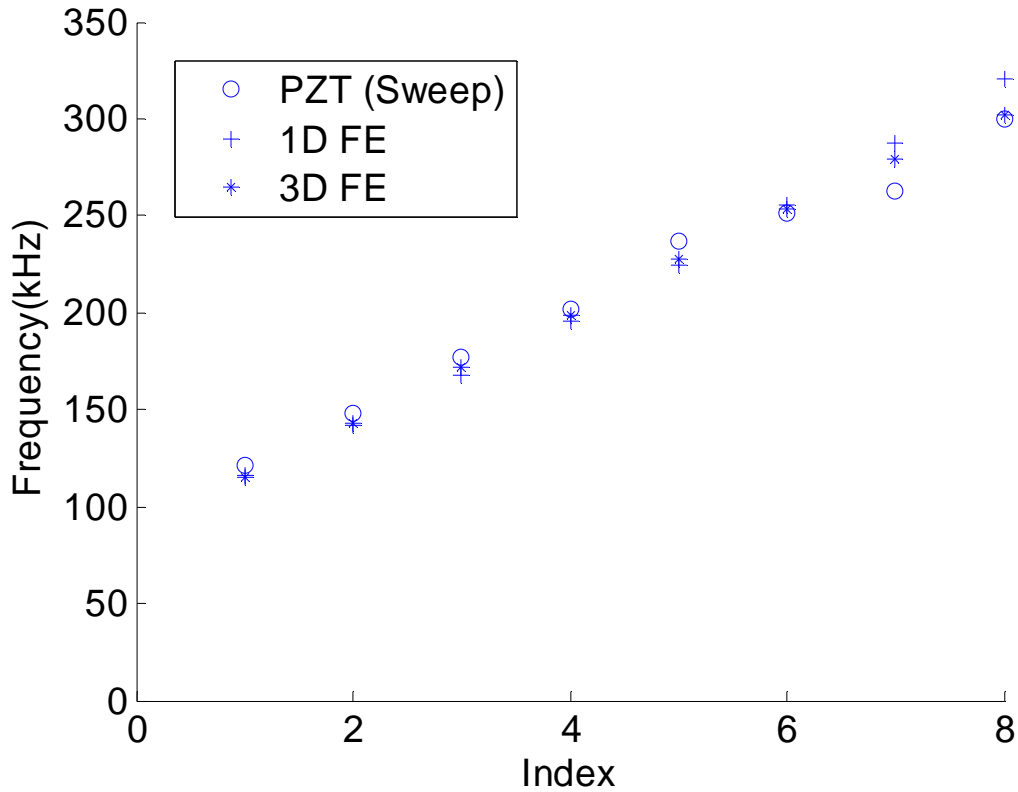


Figure 3f.6: Frequencies of modes detected in experiment compared to those seen in 1D and 3D models of the system.

In conclusion: model data was very useful in the application of the signal processing tools used experimentally for intermodulation experiments and for qualitative insights in to the behaviour of the samples, but attempts to develop a more quantitative approach were undermined by an unfortunate choice of test samples.

## **D6.4 Simulation and theoretical support for WP1 experiments: Innovative filtering techniques**

### **(4a) Phase coded pulse-sequence method (or pulse inversion method)**

An alternative filtering technique, used in the Time Reversal (TR) process (see D7), is based on the following observation. The phase inversion of a pulsed excitation signal ( $180^\circ$  phase shift) will lead to the exactly phase inverted response signal within a linear medium. However, this is not the case in a nonlinear (or microdamaged) material due to the generation of harmonics. We can take advantage of this by adding the responses from two phase-inverted pulses (positive and negative) and injecting in the backward propagation of the TR process the sum at the receivers. We call this operation ‘phase-coded pulse-sequence (PC-PS) addition’. The sum makes sure that all information on the linear scatterers is filtered out of the signal before time reversing it. Doing so, only the relevant information on the local nonlinearities is reversed and sent back into the material. The filtered energy will focus on its sources, i.e. the microdamaged zone.

### **(4b) Scaling Subtraction method**

A common feature of the nonlinear acoustic response, especially when the material is affected by damage at its early stages, is the low amplitude of the individual higher-order components and/or sideband signals. Quite often, these signals are submerged within the noise and are difficult to detect unless receivers are located close to the nonlinear scatterers.

To increase the signal-to-noise ratio of the detected nonlinear signature, we propose the Scaling Subtraction method (SSM) which exploits the nonlinear contribution to the attenuation of the fundamental harmonic component of the detected signal.

Formally, given a pure tone excitation with amplitude  $A$  and at frequency  $\omega_0$ , the received signal  $v(t)$  can be expressed in a very general form as

$$v_A(t) = \sum B_n(A) \sin(n\omega_0 t + \varphi_n(A)) \quad (4b.1)$$

In the limit of small  $A$ , the nonlinear contributions are negligible and we obtain a linear signal, considered here as the reference signal

$$v_{lin}(t) = B_{1,0} \sin(\omega_0 t + \phi_{1,0}) \quad (4b.2)$$

In our approach, we excite the specimen with a low amplitude  $A_{lin}$  and detect the reference signal  $v_{lin}$ . Then, we excite the sample with a larger amplitude  $A = kA_{lin}$ , detecting a signal  $v_A$  in the form of Eq. (4b.1) Subtraction of Eqs.(4b.1) and (4b.2), we obtain the nonlinear response as

$$w(t) = v_A(t) - \frac{A}{A_0} v_{A_0}(t) \tag{4b.3}$$

$$w(t) = \left( B_1(A) \cos(\omega_0 t + \phi_1(A)) - B_{1,0} \cos(\omega_0 t) \right) + \sum_{n=2}^{\infty} B_n(A) \sin(n\omega_0 t + \phi_n(A))$$

It can be noted that  $w$  contains the higher order harmonics of  $v_A$  plus a contribution at  $\omega_0$ , with amplitude that is dependent on the phase and on the nonlinear attenuation. Of course,  $w$  vanishes except for noise effects if the material is perfectly linear.

Evidently,  $w$  has a much larger amplitude than that of a bandpass filtered signal, which identifies nonlinear features through a signal

$$w_F(t) = \sum_{n=2}^{\infty} B_n(A) \sin(n\omega_0 t + \phi_n(A)) \tag{4b.4}$$

Besides the noticeable increase in amplitude due to the component at  $\omega_0$ , we also notice that  $w$  has the additional advantage of being derived by a simple subtraction method. On the contrary, the filtering process is always based on a complex mathematical approach, where the results are often influenced by the choices of the length and sampling of the signal and by the choice of the windowing procedures.

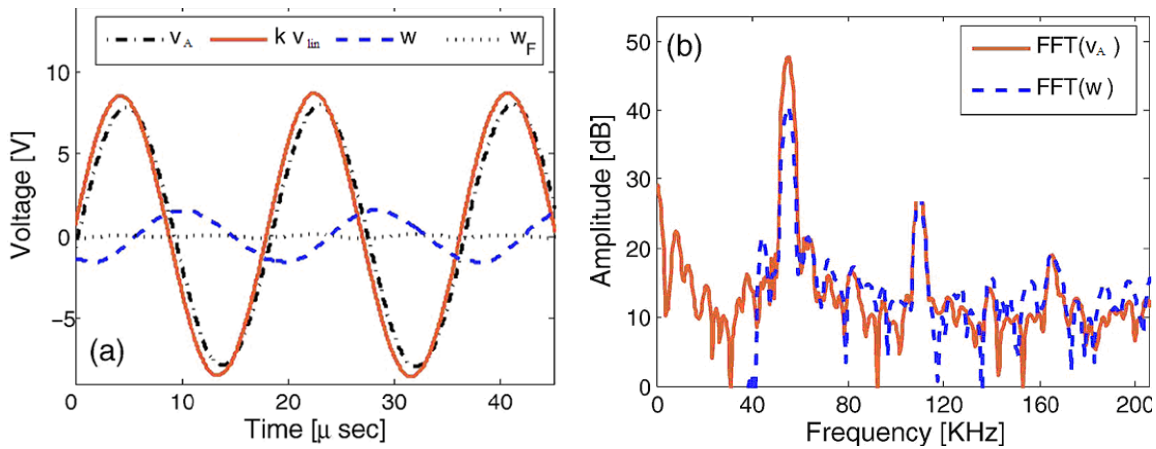


**Figure 4.1:** On the left: Recorded signals in the time domain at the lower (solid red line) and higher (dashed-dotted black line) input amplitudes. The signature of the nonlinearity is given by the difference of the two (dashed blue line) or by the filtered signal (dotted black line). On the right: FFT analysis of the recorded signal at the higher amplitude and of the subtracted signal.